

# $\eta'$ meson from two flavor dynamical domain wall fermions

Koichi HASHIMOTO<sup>1,2</sup> and Taku IZUBUCHI<sup>1,3</sup>  
(for the RBC collaboration)

<sup>1</sup>*Institute for Theoretical Physics, Kanazawa University, Kakuma,  
Kanazawa 920-1192, Japan*

<sup>2</sup>*Radiation Laboratory, RIKEN, Wako, Saitama 351-0198, Japan*

<sup>3</sup>*RIKEN-BNL Research Center, Brookhaven National Laboratory, Upton,  
NY 11973, USA*

## Abstract

We explore the spectrum of a flavor singlet pseudoscalar meson,  $\eta'$ , in two-flavor ( $N_f = 2$ ) lattice Quantum Chromo Dynamics (QCD). The continuum-like relation between the topology of the QCD vacuum and the  $U(1)_A$  anomaly, which prevents the  $\eta'$  meson from being a Nambu-Goldstone boson, is expected to hold in the domain wall fermions (DWF) used as a lattice quark field in this work. Although our simulation is limited to relatively heavy quark masses and the statistical error is not small despite the improvements in the measurements and fitting procedures for meson propagators, we obtained  $m_{\eta'} = 819(127)$  MeV for the  $N_f = 2$  QCD, where the error is only statistical. Several sources of systematic errors, which may be significant, are discussed. Results for the other mesons are also reported.

## §1. Introduction

One of the most fascinating puzzles in the meson mass spectrum is  $U(1)_A$  problem: why the mass of the flavor singlet pseudoscalar meson,  $\eta'$ , is so heavier,  $m_{\eta'} = 957.78(14)$  MeV, than that of its flavor nonsinglet counterparts in nature,  $m_{\pi^0} = 134.9766(6)$  MeV,  $m_{K^0} = 497.648(22)$  MeV, and  $m_\eta = 547.51(18)$  MeV.<sup>1)</sup>

Nonsinglet mesons behave as Nambu-Goldstone (NG) bosons with the spontaneous breaking of  $SU(3)_A$  symmetry in the quark massless limit ( $m_{\text{quark}} \rightarrow 0$ ), ignoring the small QED effects whereas  $\eta'$  is not an NG boson because  $U(1)_A$  symmetry is broken by the quantum effect, the  $U(1)_A$  anomaly. The nonvanishing divergence of the flavor singlet axial current,  $\mathcal{A}_\mu^0(x)$ , in the axial Ward-Takahashi identity (AWTI) occurs for an operator  $\mathcal{O}$  in the case of degenerate quarks up to the contact term,

$$\partial_\mu \langle \mathcal{A}_\mu^b(x) \mathcal{O} \rangle = 2m_{\text{quark}} \langle P^a(x) \mathcal{O} \rangle + \delta_{b,0} 2N_f \langle \rho_{\text{top}}(x) \mathcal{O} \rangle, \quad (1.1)$$

and expresses the anomalous breaking of chiral symmetry in the last term, which is proportional to the topological charge density,  $\rho_{\text{top}}(x)$ . For a sufficiently smooth gauge field,

$$\rho_{\text{top}}(x) = \frac{1}{32\pi^2} \epsilon_{\mu\nu\rho\sigma} \text{tr} F_{\mu\nu} F_{\rho\sigma}(x). \quad (1.2)$$

The difference in the pseudoscalar meson masses between the flavor singlet sector,  $m_{\eta'}$ , and the non-singlet sector,  $m_\pi$ , was estimated by the Witten-Veneziano (WV) relation,<sup>2),3)</sup>

$$m_0^2 = m_{\eta'}^2 - m_\pi^2 = \frac{2N_f}{f_\pi^2} \chi_{\text{top}} \quad (1.3)$$

at the limit of  $N_c \rightarrow \infty$ . Here  $\chi_{\text{top}}$  is the susceptibility of the topological charge ( $Q_{\text{top}}$ ) :

$$\chi_{\text{top}} = \frac{\langle Q_{\text{top}}^2 \rangle}{VT}, \quad Q_{\text{top}} = \int \rho_{\text{top}}(x) d^4x, \quad (1.4)$$

in pure Yang-Mills (YM) theory in a four dimensional volume  $VT$ . A recent result in  $N_c = 3$  YM theory with the overlap fermion<sup>4)</sup> shows that  $\chi = (191(5)\text{MeV})^4$ .  $\eta'$  mass from this estimation for  $N_f = 3$  and in the chiral limit,  $m_\pi^2 \rightarrow 0$ , is  $m_{\eta'} \approx 970$  MeV, which is very close to experimental values.

The direct numerical calculation of the  $\eta'$  spectrum is important for checking theoretical scenarios such as the WV relation, and should result in its correction in finite  $N_c$  and nonzero quark masses.

Simulations of  $\eta'$  physics in pure YM theory with quenched Wilson fermions were carried out in pioneer works.<sup>5),6)</sup> The relation between the topological charge and the mass of  $\eta'$

was also explored.<sup>7)</sup> Unquenched simulations<sup>8)-12)</sup> were performed for two-flavor and for 2+1-flavor<sup>13)</sup> of Wilson fermions. Using staggered fermions,  $m_{\eta'}$  has been calculated for  $N_f = 0, 2$ <sup>14)</sup> and  $N_f = 2 + 1$ .<sup>47),48)</sup> Recently there are other interesting investigations, such as using twisted-mass quarks<sup>49)</sup> or a local imaginary  $\theta$ -term.<sup>50)</sup>

In this paper, we discuss the mass of  $\eta'$  in  $N_f = 2$  QCD with domain wall fermions (DWF). DWF<sup>18)-20)</sup> is one of the lattice chiral fermions, which has both flavor and chiral symmetries even at finite lattice spacing ( $a > 0$ ), and is thus suitable for investigation of nonperturbative physics of chiral anomalies. These features of DWF make their use preferable to the other alternative methods of discretization. Wilson fermions break chiral symmetry at  $a > 0$  and discretization errors start at  $\mathcal{O}(a\Lambda_{\text{QCD}})$ . The singlet flavor meson in staggered fermions is a very important subject as it may be related to the potential issue about the locality of the formalisms in the continuum limit.<sup>16),17)</sup>

Chiral and flavor symmetry are particularly important for  $\eta'$  physics, and the DWF is the natural choice of lattice quark in investigations. Chiral symmetry in a DWF is not realized perfectly, it is broken due to its finite extent in the fifth direction,  $L_s$ . The amount of breaking can be measured by a shift in quark mass:  $m_{\text{quark}} = m_f + m_{\text{res}}$ , so that the nonsinglet axial current is conserved at  $m_{\text{quark}} = 0$ .  $m_{\text{res}}$  is called the residual quark mass and vanishes at large  $L_s$  for a sufficiently smooth gauge configuration.<sup>21)</sup>

Although it is desirable to take  $L_s \rightarrow \infty$  limit, to reduce the computational cost, we restrict ourselves to finite  $L_s = 12$  with the combination of DBW2 improved gauge action,<sup>22),23)</sup> which smoothen gauge field at short distance and reduces  $m_{\text{res}}$  significantly.<sup>24)</sup>

The RBC collaboration examined the first large scale dynamical DWF simulation.<sup>25)</sup> Pseudoscalar meson masses and decay constants were computed and fit to the chiral perturbation theory (ChPT) formula.  $m_\pi$ ,  $m_K$ ,  $m_\rho$ ,  $f_\pi$ , and  $f_K$  calculated in their work are reasonably consistent with values obtained in experiments. The  $J$  parameter is closer to the phenomenological value than the value obtained in the quenched simulation. The nonsinglet scalar meson,  $a_0$ , mass and the decay constant have also been examined both in dynamical QCD and partially quenched QCD using partially quenched ChPT.<sup>26)</sup>

We will mainly focus on the  $\eta'$  meson in this paper, but we will also report on the results of other mesons belong to other Lorentz and flavor representations, and also investigate the signal of the mesons in their excited state and their decay constants.

As the results are limited to the isospin symmetric case and the number of dynamical quarks is two, our focal interest in this paper is to provide a benchmark calculation for the study of the general meson spectrum on a dynamical DWF ensemble with various (smeared) meson field using a larger statistical sample than in the previous study.

In §2, the theoretical expectations of  $\eta'$  meson physics are summarized. We explain the

details of the simulation including improvements in the signal-to-noise ratio and the fitting methods used to relate the simulation data to physical quantities in §3. The numerical results are presented in §4 with a list of their systematic uncertainties. We will summarize in §5.

## §2. Theoretical results on physics of flavor singlet meson

In (continuum Euclidean) QCD with  $N_f$  degenerated quarks, the operator of the flavor singlet pseudoscalar meson,  $\eta'$ :  $I(J^P) = 0(0^-)$ , is defined by quark operators,  $q_f$ , as

$$\eta'(x) = \frac{1}{\sqrt{N_f}} \sum_{f=1}^{N_f} \bar{q}_f(x) i\gamma_5 q_f(x), \quad (2.1)$$

where  $f = 1, \dots, N_f$  is the flavor index. The  $\eta'$  propagator consists of two parts:

$$\begin{aligned} \int d^3x \langle \eta'(\vec{x}, t) \eta'^{\dagger}(\vec{0}, 0) \rangle &= C_{\gamma_5}(t) - N_f D_{\gamma_5}(t), \\ C_{\gamma_5}(t) &= - \int d^3x \left\langle \frac{1}{N_f} \sum_f \overbrace{\bar{q}_f(\vec{x}, t) \gamma_5 q_f(\vec{x}, t) \bar{q}_f(\vec{0}, 0) \gamma_5 q_f(\vec{0}, 0)} \right\rangle, \\ D_{\gamma_5}(t) &= \int d^3x \left\langle \frac{1}{N_f} \sum_f \overbrace{\bar{q}_f(\vec{x}, t) \gamma_5 q_f(\vec{x}, t)} \frac{1}{N_f} \sum_g \overbrace{\bar{q}_g(\vec{0}, 0) \gamma_5 q_g(\vec{0}, 0)} \right\rangle. \end{aligned} \quad (2.2)$$

The braces represent the contraction of the quark propagators,  $S_q(0, t)$ . Thus, for example,  $C_{\gamma_5}(t)$  is  $\langle S_q(t, 0) \gamma_5 S_q(0, t) \gamma_5 \rangle$ , the same as the nonsinglet meson (pion) propagator, and  $D_{\gamma_5}(t)$  is the correlation function between disconnected quark loops, which exists in the flavor singlet mesons. When  $D_{\gamma_5}(t)$  is suppressed by the OZI rule, it propagates and acquires  $U(1)_A$  anomaly.

In dynamical QCD, in which the mass of quark polarizing the gluon,  $m_{\text{sea}}$ , is equal to that of the valence quark consisting the meson operator,  $m_{\text{val}}$ , the  $\eta'$  propagator is an exponential function of time with its damping factor being the mass of the meson,  $m'_{\eta'}$ ,

$$\int d^3x \langle \eta'(\vec{x}, t) \eta'^{\dagger}(\vec{0}, 0) \rangle = C_{\gamma_5}(t) - N_f D_{\gamma_5}(t) = A_{\eta'} e^{-m_{\eta'} t} + \dots, \quad (2.3)$$

at large  $t$ .

A model of the  $\eta'$  propagator is depicted in Fig. 1. The meson propagator is expressed as a series expansion in number of the quark loops with signs reflecting the Grassmannian feature of the quark, and the blobs at the ends are the meson operators (2.1). The wavy lines connecting the quark loops represent the coupling between disconnected loops attached to the pseudoscalar density, which is related to the  $U(1)_A$  anomaly.

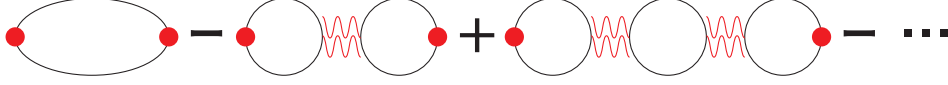


Fig. 1. Diagram of  $\eta'$  propagator.

The meson propagator in momentum space can be calculated from the model. The first term in Fig. 1 is the same as the nonsinglet pseudoscalar meson (pion),  $1/(p^2 + m_\pi^2)$ , and the second term is given by two pion propagators coupled to each other by gluons,  $1/(p^2 + m_\pi^2) \times m_0^2/N_f \times 1/(p^2 + m_\pi^2)$ , whose coupling we parameterize as  $m_0^2/N_f$ . There are  $N_f$  combinations of quark loops in the second term. Repeating the similar identification of connected pion propagators to the  $n$ th order, the momentum space representation of the  $\eta'$  propagator can be written as a geometrical series:

$$\begin{aligned}
& \langle \eta'(p) \eta'^\dagger(-p) \rangle \\
& \propto \frac{1}{p^2 + m_\pi^2} - N_f \frac{1}{p^2 + m_\pi^2} \frac{m_0^2}{N_f} \frac{1}{p^2 + m_\pi^2} + N_f^2 \frac{1}{p^2 + m_\pi^2} \frac{m_0^2}{N_f} \frac{1}{p^2 + m_\pi^2} \frac{m_0^2}{N_f} \frac{1}{p^2 + m_\pi^2} - \dots \\
& = \frac{1}{p^2 + m_\pi^2} \sum_{n=0}^{\infty} \left( \frac{-m_0^2}{p^2 + m_\pi^2} \right)^n = \frac{1}{p^2 + (m_\pi^2 + m_0^2)}, \tag{2.4}
\end{aligned}$$

The  $m_\pi$  pole in the connected diagram,  $C_{\gamma_5}$ , is exactly canceled by part of the disconnected diagram,  $D_{\gamma_5}$ , and thus the square of the  $\eta'$  meson mass,  $m_{\eta'}^2$ , is identified by  $m_\pi^2 + m_0^2$ , which means  $\eta'$  does not behave as an NG boson. In terms of this model,  $\eta'$  spectroscopy calculated in lattice simulation should reveal the magnitude of  $m_0^2$ , and if it is consistent with the WV relation (1.3).

In a later section, we will also calculate the ratio between  $D_{\gamma_5}(t)$  and  $C_{\gamma_5}(t) \sim A_\pi e^{-m_\pi t}$ . From (2.3), the ratio at large  $t$  should behave as

$$\frac{N_f D_{\gamma_5}(t)}{C_{\gamma_5}(t)} = 1 - B \frac{e^{m_{\eta'} t} + e^{-m_{\eta'}(T-t)}}{e^{m_\pi t} + e^{-m_\pi(T-t)}} + \dots \tag{2.5}$$

$$\stackrel{(T-t) \gg 1}{\longrightarrow} 1 - B e^{-\Delta m t} + \dots, \tag{2.6}$$

$$\Delta m = m_{\eta'} - m_\pi, \quad B = \frac{A_{\eta'}}{A_\pi}. \tag{2.7}$$

The ratio at large  $t$  exponentially approaches unity with the exponent being the mass difference between  $\eta'$  and pion, which is a signature of the dynamical sea quark. This is in contrast to the quenched QCD, in which  $m_{\text{sea}}$  is taken to be infinitely heavy while  $m_{\text{val}}$  is kept finite. In this nonunitary theory, the third and higher terms in the quark loop expansion (2.3) are missing due to the decoupling of the sea quark, and the resulting meson propagator

has an unphysical double pole,

$$\langle \eta'(p) \eta'^{\dagger}(-p) \rangle_{\text{quenched}} \propto \frac{1}{p^2 + m_{\pi}^2} - N_f \frac{1}{p^2 + m_{\pi}^2} \frac{m_0^2}{N_f} \frac{1}{p^2 + m_{\pi}^2}. \quad (2.8)$$

The ratio  $D_{\gamma_5}(t)/C_{\gamma_5}(t)$  in this case behaves as a linear function of time,

$$\frac{N_f D_{\gamma_5}^{(\text{quenched})}(t)}{C_{\gamma_5}(t)} = \frac{m_0^2}{2m_{\pi}} t + \text{const} + \dots, \quad (2.9)$$

which is clearly different from (2.6). Thus, to obtain a physical  $\eta'$  we must simulate the dynamical theory ( $m_{\text{sea}} = m_{\text{val}}$ ). We will examine  $m_{\eta'}$  in the domain wall QCD only at the dynamical points.

### §3. Simulation details

#### 3.1. Domain wall fermion (DWF)

The DWF action is defined as

$$S_F = \sum_{x,y,s,s'} \bar{\psi}(x,s) D_{\text{DWF}}(x,s;y,s') \psi(y,s'), \quad (3.1)$$

$$D_{\text{DWF}}(x,s;y,s') = \delta_{s,s'} D_{x,y}^{\parallel} + \delta_{x,y} D_{s,s'}^{\perp}, \quad (3.2)$$

$$D_{x,y}^{\parallel} = \frac{1}{2} \sum_{\mu=1}^4 [(1 - \gamma_{\mu}) U_{\mu}(x) \delta_{x+\hat{\mu},y} + (1 + \gamma_{\mu}) U_{\mu}^{\dagger}(y) \delta_{x-\hat{\mu},y}] + (M_5 - 4) \delta_{x,y}, \quad (3.3)$$

$$D_{s,s'}^{\perp} = \frac{1}{2} [(1 - \gamma_5) \delta_{s+1,s'} + (1 + \gamma_5) \delta_{s-1,s'}] + \frac{m_f}{2} [(1 - \gamma_5) \delta_{s,L_s-1} \delta_{0,s'} + (1 + \gamma_5) \delta_{s,0} \delta_{L_s-1,s'}], \quad (3.4)$$

where  $\psi(x,s)$  is a DWF that is located in five dimensional space,  $(x,s)$ ,  $L_s$  is the size of the fifth direction, and the parameter  $M_5$  is the domain wall height. By setting  $M_5$  in a region around  $[0, 2]$ , from (3.4), left-(right-)handed zero modes are localized around  $s = 0(L_s - 1)$  and the zero modes undergo exponential damping as  $s$ ,  $(L_s - 1 - s)$  increases. When a four-dimensional fermion and antifermion,  $q(x)$  and  $\bar{q}(x)$ , are defined as

$$q(x) = \frac{1 - \gamma_5}{2} \psi(x, 0) + \frac{1 + \gamma_5}{2} \psi(x, L_s - 1), \quad (3.5)$$

$$\bar{q}(x) = \bar{\psi}(x, 0) \frac{1 + \gamma_5}{2} + \bar{\psi}(x, L_s - 1) \frac{1 - \gamma_5}{2}, \quad (3.6)$$

chiral symmetry is fulfilled even with finite lattice spacing ( $a > 0$ ) at the  $L_s \rightarrow \infty$  limit.

However, in the simulation,  $L_s$  is restricted to be finite, and the AWTI is modified from its expression in the continuum theory to,

$$\partial_{\mu} \langle \mathcal{A}_{\mu}^b(x) \mathcal{O} \rangle = 2(m_f + m_{\text{res}}) \langle P^b(x) \mathcal{O} \rangle, \quad (3.7)$$

i.e., the physical quark mass is shifted to  $m_{\text{quark}} = m_f + m_{\text{res}}$ .  $m_{\text{res}}$  is a small lattice artifact called the residual quark mass, defined as

$$m_{\text{res}} = \lim_{t \rightarrow \infty} \frac{\sum_{\vec{x}} \langle J_{5q}^b(\vec{x}, t) P^b(\vec{0}, 0) \rangle}{\sum_{\vec{x}} \langle P^b(\vec{x}, t) P^b(\vec{0}, 0) \rangle}, \quad (3.8)$$

where  $J_{5q}^b(\vec{x}, t)$  is an operator similar to the pseudoscalar operator but made of fermions at the midpoint of the fifth direction,<sup>20)</sup>  $s \sim L_s/2$ , thus the numerator of (3.8) includes the contractions between the surface fermions at  $s = 0$  or  $s = L_s$  and the midpoint fermions at  $s \sim L_s/2$ . For the flavor non-singlet case,  $b \neq 0$ ,  $m_{\text{res}}$  is an exponential function of  $L_s$  as a consequence of the exponentially localized zero modes to the surface, and vanishes as  $L_s \rightarrow \infty$ .

One could further argue<sup>52)</sup> that the effective Lagrangian contains the diverging,  $\mathcal{O}(1/a)$ , discretization error, which can be corrected by the small shift of the quark mass,  $m_{\text{quark}} = m_f + m_{\text{res}}$ . The remaining error is  $\mathcal{O}(a)$ , similar to that of Wilson fermions, however, it is an exponentially small number,  $e^{\alpha L_s}$ , or  $\mathcal{O}(m_{\text{res}})$ . Although  $m_{\text{res}}$  is small compared with the statistical errors we will have in most of observables, we will treat the shifted quark mass  $m_{\text{quark}} = m_f + m_{\text{res}}$  as the physical quark mass so that our analysis is precise modulo  $\mathcal{O}(m_{\text{res}} a, a^2)$ , which is a few percent in our simulation.

On the other hand, for flavor singlet ( $b = 0$ ) case,  $J_{5q}^b(\vec{x}, t)$  in (3.8) can be attached to a quark loop that does not propagate in the entire  $L_s$  in the fifth direction, and is free from suppression. the counterparts of  $m_{\text{res}}$  in the flavor singlet case remains finite even as  $L_s \rightarrow \infty$ , and reproduces the following anomalous term<sup>51)</sup>

$$\sum_{\vec{x}} \langle J_{5q}^b(\vec{x}, t) \mathcal{O} \rangle \rightarrow \delta_{b,0} \sum_{\vec{x}} \langle \rho_{\text{top}}(\vec{x}, t) \mathcal{O} \rangle. \quad (3.9)$$

In summary, DWF even for finite  $L_s$  correctly reproduces the quantum anomaly of axial symmetry with small error due to lattice discretization.

### 3.2. Ensemble: actions and parameters

We employ the  $N_f = 2$  QCD ensemble<sup>25)</sup> with DWF actions described in the previous subsection. Our gauge action contains an improvement in the sense of the renormalization group invariance, DBW2:<sup>23)</sup>

$$S_G = \frac{\beta}{3} \left[ (1 - 8c_1) \sum_{x, \mu > \nu} \text{ReTr}[1 - P_{\mu\nu}(x)] + c_1 \sum_{x, \mu \neq \nu} \text{ReTr}[1 - R_{\mu\nu}(x)] \right], \quad (3.10)$$

$$P_{\mu\nu}(x) = U_\mu(x) U_\nu(x + \hat{\mu}) U_\mu^\dagger(x + \hat{\nu}) U_\nu^\dagger(x), \quad (3.11)$$

$$R_{\mu\nu}(x) = U_\mu(x) U_\mu(x + \hat{\mu}) U_\nu(x + 2\hat{\mu}) U_\mu^\dagger(x + \hat{\mu} + \hat{\nu}) U_\mu^\dagger(x + \hat{\nu}) U_\nu^\dagger(x), \quad (3.12)$$

Table I. Lattice ensembles and simulation parameters.

$\beta$	$c_1$	$V \times T$	$a^{-1}$ [GeV]	$a$ [fm]	$Va^3$ [fm <sup>3</sup> ]	$m_{\text{res}}$
0.80	-1.4069	$16^3 \times 32$	1.537(26)	0.1284(22)	$(2.054)^3$	0.00137(4)
$m_f$	$m_\pi/m_\rho$	begin-end(step) traj.			#config.	$N_{\text{noise}}$
0.02	0.5121(36)	656-5351(5)			940	1
0.03	0.5984(31)	615-6205(10)			560	3
0.04	0.6415(33)	625-1765(10), 2075-5615(10) <sup>a</sup>			470	2

<sup>(a)</sup> For the  $m_f = 0.04$  ensemble, we do not use trajectories 1775-2065 due to a hardware error on trajectory 1772 that was not detected until lattice generation was finished.

with  $\beta = 0.80$  and  $c_1 = -1.4069$ . The parameters of the DWF action (3.4) are set as  $L_s = 12$  and  $M_5 = 1.8$ . We measure observables on a 470-940 lattice configuration samples for three different masses,  $m_f=0.02$ , 0.03, and 0.04, which correspond to  $m_\pi/m_\rho \approx 0.51$ -0.64. The lattice size is  $16^3 \times 32$ , the lattice scale is  $a^{-1} \approx 1.5$  GeV ( $a \approx 0.13$  fm), and the residual chiral breaking  $m_{\text{res}} = 0.00137(4)$  which is about an order of magnitude smaller than the input quark masses. Throughout this paper we estimate the statistical error using the blocked jackknife method. The size of the block is determined to be 50 trajectories by monitoring the autocorrelation of the hadron propagators. A summary of lattice ensembles and parameters is given in Table I. Other results on these ensembles can be found in 25), 26), 30)–32).

### 3.3. Improvements: smearing and sources

Before constructing the meson propagators, we describe an improvement for the quark propagators in this section. It is known to be difficult to reduce the statistical error of the flavor singlet meson spectrum. As we have seen in the previous section, the meson propagator includes the correlation function between disconnected loops,  $D_\Gamma$  ( $\Gamma = \gamma_5, \gamma_i, \mathbf{1}, \gamma_5\gamma_i, \gamma_i\gamma_j$ ), whose statistical fluctuation is very large, particularly for large  $t$  as we will see. We have implemented smearing for a quark operator in a gauge-covariant manner called Wuppertal smearing.<sup>27)</sup> The smeared quark operator  $q_S$  is a gauge-covariant superposition of the local quark operator  $q_L$ :

$$q_L^c(\vec{x}, t) \rightarrow q_S^c(\vec{x}, t) = \sum_{\vec{y}, c'} F^{c, c'}(\vec{x}, \vec{y}) q_L^{c'}(\vec{y}, t), \quad (3.13)$$

$$F^{c, c'}(\vec{x}, \vec{y}) = \left[ \left\{ \mathbf{1} + \frac{\omega^2}{4N} \sum_{i=1}^3 (\nabla_i + \nabla_i^\dagger) \right\}^N \right]_{\vec{x}, c; \vec{y}, c'}, \quad (3.14)$$

$$[\mathbf{1}]_{\vec{x}, c; \vec{y}, c'} = \delta^{c, c'} \delta_{\vec{x}, \vec{y}}, \quad (3.15)$$

$$[\nabla_i]_{\vec{x}, c; \vec{y}, c'} = U_i(\vec{x}, t)^{c, c'} \delta_{\vec{x}+\hat{i}, \vec{y}} - \delta^{c, c'} \delta_{\vec{x}, \vec{y}}, \quad (3.16)$$



$$[\nabla_i^\dagger]_{\vec{x},c;\vec{y},c'} = U_i^\dagger(\vec{y},t)^{c,c'} \delta_{\vec{x}-\hat{i},\vec{y}} - \delta^{c,c'} \delta_{\vec{x},\vec{y}}. \quad (3.17)$$

The shape of  $q_S$  in terms of  $q_L$  is Gaussian with width  $\omega$  as  $N \rightarrow \infty$ . We set  $\omega = 4.35$  and  $N = 40$ . The overlap between the ground state and the meson operator made of smeared quarks is expected to be larger the meson made of unsmeared quarks, and the excited state contamination is suppressed for small  $t$ , where the statistical error is smaller.

Both the quark correlation functions,  $C_\Gamma(t)$  and  $D_\Gamma(t)$ , are calculated for a complex  $\mathbf{Z}_2$  noise source,  $\xi$ , defined by

$$\xi^{(n)}(\vec{x},t) = \frac{1}{\sqrt{2}}[\xi_1^{(n)}(\vec{x},t) + i\xi_2^{(n)}(\vec{x},t)], \quad (3.18)$$

where  $n = 1, 2, \dots, N_{\text{noise}}$  are random noise ensembles and  $\xi_1$  and  $\xi_2$  take values of  $\pm 1$  randomly.  $\xi(\vec{x},t)$  is statistically independent of space-time: thus, it satisfies

$$\lim_{N_{\text{noise}} \rightarrow \infty} \frac{1}{N_{\text{noise}}} \sum_{n=1}^{N_{\text{noise}}} \xi^{(n)}(\vec{x},t) \xi^{(n)}(\vec{y},t') = 0, \quad (3.19)$$

$$\lim_{N_{\text{noise}} \rightarrow \infty} \frac{1}{N_{\text{noise}}} \sum_{n=1}^{N_{\text{noise}}} \xi^{(n)}(\vec{x},t) \xi^{(n)*}(\vec{y},t') = \delta_{\vec{x},\vec{y}} \delta_{t,t'}, \quad (3.20)$$

which is useful for calculating the disconnected loops as we will see in the next subsection. We use the source restricted to a time slice (wall source) for  $C_\Gamma(t)$  and a space-time volume source for  $D_\Gamma(t)$ , and  $N_{\text{noise}} = 1, 3$ , and  $2$  for  $m_f=0.02, 0.03$ , and  $0.04$ , respectively.

### 3.4. Meson operators and correlation functions

Our naming convention for meson fields is similar to that used by the particle data group,<sup>1)</sup> but our simulation is limited to having only up and down quarks ( $N_f = 2$ ) with degenerate masses and zero electric charges; thus, the meson spectra are inevitably different from those in the real world. The systematic error from these omission may be comparable or smaller to our target precision of  $\sim 10\%$ . This point certainly needs further investigation.

The Hermitian interpolation fields for flavor nonsinglet meson in our simulation,  $\pi$ ,  $\rho$ ,  $a_0$ ,  $a_1$ , and  $b_1$ , and singlet fields,  $\eta'$ ,  $\omega$ ,  $f_0$ ,  $f_1$ , and  $h_1$  are defined in terms of quark operators,  $q_{I,f}$  and  $\bar{q}_{J,f}$  as follows:

$$\pi_I(\vec{x},t) = \frac{1}{\sqrt{2}} \sum_{f,g=1}^2 \bar{q}_{I,f}(\vec{x},t) \tau_{f,g}^b i\gamma_5 q_{I,g}(\vec{x},t), \quad (3.21)$$

$$\rho_I(\vec{x},t) = \frac{1}{\sqrt{6}} \sum_{i=1}^3 \sum_{f,g=1}^2 \bar{q}_{I,f}(\vec{x},t) \tau_{f,g}^b i\gamma_i q_{I,g}(\vec{x},t) \quad (3.22)$$

Table II. Meson operators in the simulation and their quantum numbers.

Meson type	$J^{PC}$	$\Gamma$	nonsinglet	singlet
pseudoscalar	$0^{-+}$	$i\gamma_5$	$\pi$	$\eta'$
vector	$1^{--}$	$i\gamma_i^a$	$\rho$	$\omega$
scalar	$0^{++}$	$\mathbf{1}$	$a_0$	$f_0$
pseudovector	$1^{++}$	$i\gamma_5\gamma_i^a$	$a_1$	$f_1$
pseudovector	$1^{+-}$	$i\gamma_i\gamma_j^a$	$b_1$	$h_1$

<sup>(a)</sup> average over  $i, j = 1, 2, 3$  is taken.

$$a_{0I}(\vec{x}, t) = \frac{1}{\sqrt{2}} \sum_{f,g=1}^2 \bar{q}_{I,f}(\vec{x}, t) \tau_{f,g}^b q_{I,g}(\vec{x}, t), \quad (3.23)$$

$$a_{1I}(\vec{x}, t) = \frac{1}{\sqrt{6}} \sum_{i=1}^3 \sum_{f,g=1}^2 \bar{q}_{I,f}(\vec{x}, t) \tau_{f,g}^b i\gamma_5 \gamma_i q_{I,g}(\vec{x}, t) \quad (3.24)$$

$$b_{1I}(\vec{x}, t) = \frac{1}{\sqrt{6}} \sum_{\substack{1 \leq i \leq 3 \\ i < j \leq 3}} \sum_{f,g=1}^2 \bar{q}_{I,f}(\vec{x}, t) \tau_{f,g}^b i\gamma_i \gamma_j q_{I,g}(\vec{x}, t) \quad (3.25)$$

$$\eta'_I(\vec{x}, t) = \frac{1}{\sqrt{2}} \sum_{f=1}^2 \bar{q}_{I,f}(\vec{x}, t) i\gamma_5 q_{I,f}(\vec{x}, t), \quad (3.26)$$

$$\omega_I(\vec{x}, t) = \frac{1}{\sqrt{6}} \sum_{i=1}^3 \sum_{f=1}^2 \bar{q}_{I,f}(\vec{x}, t) i\gamma_i q_{I,f}(\vec{x}, t) \quad (3.27)$$

$$f_{0I}(\vec{x}, t) = \frac{1}{\sqrt{2}} \sum_{f=1}^2 \bar{q}_{I,f}(\vec{x}, t) q_{I,f}(\vec{x}, t), \quad (3.28)$$

$$f_{1I}(\vec{x}, t) = \frac{1}{\sqrt{6}} \sum_{i=1}^3 \sum_{f=1}^2 \bar{q}_{I,f}(\vec{x}, t) i\gamma_5 \gamma_i q_{I,f}(\vec{x}, t) \quad (3.29)$$

$$h_{1I}(\vec{x}, t) = \frac{1}{\sqrt{6}} \sum_{\substack{1 \leq i \leq 3 \\ i < j \leq 3}} \sum_{f=1}^2 \bar{q}_{I,f}(\vec{x}, t) i\gamma_i \gamma_j q_{I,f}(\vec{x}, t) \quad (3.30)$$

where  $\tau^b$  ( $b = 1, 2, 3$ ) are the Pauli matrices for the flavor indices  $f$  and  $g$ , and  $I$  and  $J$  denotes whether we use the local quark field ( $L$ ) or the smeared field ( $S$ ) to control the ground-state overlap. In Table II, we summarize the quantum numbers of each meson field.

The two-point correlation functions between the interpolation fields are calculated as

$$\sum_{\vec{x}, \vec{y}} \langle \pi_I(\vec{x}, t) \pi_J^\dagger(\vec{y}, 0) \rangle = C_{IJ, \gamma_5}(t), \quad (3.31)$$

$$\sum_{\vec{x}, \vec{y}} \langle \rho_I(\vec{x}, t) \rho_J^\dagger(\vec{y}, 0) \rangle = \frac{1}{3} \sum_{i=1}^3 C_{IJ, \gamma_i}(t), \quad (3.32)$$

$$\sum_{\vec{x}, \vec{y}} \langle a_{0I}(\vec{x}, t) a_{0J}^\dagger(\vec{y}, 0) \rangle = C_{IJ, \mathbf{1}}(t), \quad (3.33)$$

$$\sum_{\vec{x}, \vec{y}} \langle a_{1I}(\vec{x}, t) a_{1J}^\dagger(\vec{y}, 0) \rangle = \frac{1}{3} \sum_{i=1}^3 C_{IJ, \gamma_5 \gamma_i}(t), \quad (3.34)$$

$$\sum_{\vec{x}, \vec{y}} \langle b_{1I}(\vec{x}, t) b_{1J}^\dagger(\vec{y}, 0) \rangle = \frac{1}{3} \sum_{i < j} C_{IJ, \gamma_i \gamma_j}(t), \quad (3.35)$$

$$\sum_{\vec{x}, \vec{y}} \langle \eta'_I(\vec{x}, t) \eta'_J(\vec{y}, 0) \rangle = C_{IJ, \gamma_5}(t) - 2D_{IJ, \gamma_5}(t), \quad (3.36)$$

$$\sum_{\vec{x}, \vec{y}} \langle \omega_I(\vec{x}, t) \omega_J^\dagger(\vec{y}, 0) \rangle = \frac{1}{3} \sum_{i=1}^3 [C_{IJ, \gamma_i}(t) - 2D_{IJ, \gamma_i}(t)], \quad (3.37)$$

$$\sum_{\vec{x}, \vec{y}} \langle f_{0I}(\vec{x}, t) f_{0J}^\dagger(\vec{y}, 0) \rangle = C_{IJ, \mathbf{1}}(t) - 2D_{IJ, \mathbf{1}}(t), \quad (3.38)$$

$$\sum_{\vec{x}, \vec{y}} \langle f_{1I}(\vec{x}, t) f_{1J}^\dagger(\vec{y}, 0) \rangle = \frac{1}{3} \sum_{i=1}^3 [C_{IJ, \gamma_5 \gamma_i}(t) - 2D_{IJ, \gamma_5 \gamma_i}(t)], \quad (3.39)$$

$$\sum_{\vec{x}, \vec{y}} \langle h_{1I}(\vec{x}, t) h_{1J}^\dagger(\vec{y}, 0) \rangle = \frac{1}{3} \sum_{i < j} [C_{IJ, \gamma_i \gamma_j}(t) - 2D_{IJ, \gamma_i \gamma_j}(t)], \quad (3.40)$$

in terms of the connected and disconnected quark loop contributions (Tr is for the trace over color and spinor indices only):

$$\begin{aligned} C_{IJ, \Gamma}(t) &= \sum_{\vec{x}, \vec{y}} \left\langle \overbrace{\bar{q}_I(\vec{x}, t) \Gamma \bar{q}_I(\vec{x}, t) \bar{q}_J(\vec{y}, 0) \Gamma q_J(\vec{y}, 0)} \right\rangle \\ &= - \sum_{\vec{x}, \vec{y}} \langle \text{Tr} [G_{IJ}(\vec{x}, t; \vec{y}, 0) \Gamma G_{JI}(\vec{y}, 0; \vec{x}, t) \Gamma] \rangle \quad (\Gamma = i\gamma_5, i\gamma_i, \mathbf{1}, i\gamma_5 \gamma_i, i\gamma_i \gamma_j), \end{aligned} \quad (3.41)$$

$$\begin{aligned} D_{IJ, \Gamma}(t) &= - \sum_{\vec{x}, \vec{y}} \left\langle \overbrace{\bar{q}_I(\vec{x}, t) \Gamma \bar{q}_I(\vec{x}, t)} \overbrace{\bar{q}_J(\vec{y}, 0) \Gamma q_J(\vec{y}, 0)} \right\rangle \\ &= - \sum_{\vec{x}, \vec{y}} \left\langle \left\{ \text{Tr} [G_{II}(\vec{x}, t; \vec{x}, t) \Gamma] - \sum_{\vec{x}'} \langle \text{Tr} [G_{II}(\vec{x}', t; \vec{x}', t) \Gamma] \rangle \right\} \right. \\ &\quad \times \left. \left\{ \text{Tr} [G_{JJ}(\vec{y}, 0; \vec{y}, 0) \Gamma] - \sum_{\vec{y}'} \langle \text{Tr} [G_{JJ}(\vec{y}', 0; \vec{y}', 0) \Gamma] \rangle \right\} \right\rangle \\ &\quad (\Gamma = i\gamma_5, i\gamma_i, \mathbf{1}, i\gamma_5 \gamma_i, i\gamma_i \gamma_j). \end{aligned} \quad (3.42)$$

Here  $G_{IJ}(\vec{x}, t; \vec{y}, t')$  is the propagator of the four dimensional quark field

$$G_{LL}^{c, \alpha; c', \alpha'}(\vec{x}, t; \vec{y}, t') = [D^{-1}(\vec{x}, t; \vec{y}, t')]^{c, \alpha; c', \alpha'}, \quad (3.43)$$

$$G_{LS}^{c, \alpha; c', \alpha'}(\vec{x}, t; \vec{y}, t') = \sum_{c''} \sum_{\vec{x}'} [D^{-1}(\vec{x}, t; \vec{x}', t')]^{c, \alpha; c'', \alpha'} F^{c'', c'}(\vec{x}', \vec{y}), \quad (3.44)$$

$$G_{SL}^{c, \alpha; c', \alpha'}(\vec{x}, t; \vec{y}, t') = \sum_{c''} \sum_{\vec{x}'} F^{c, c''}(\vec{x}, \vec{x}') [D^{-1}(\vec{x}', t; \vec{y}, t')]^{c'', \alpha; c', \alpha'}, \quad (3.45)$$

$$G_{SS}^{c, \alpha; c', \alpha'}(\vec{x}, t; \vec{y}, t') = \sum_{c'', c'''} \sum_{\vec{x}', \vec{y}'} F^{c, c''}(\vec{x}, \vec{x}') [D^{-1}(\vec{x}', t; \vec{y}', t')]^{c'', \alpha; c''', \alpha'} F^{c''', c'}(\vec{y}', \vec{y}), \quad (3.46)$$

where  $D^{-1}$  is written in terms of the inverse of the five dimensional matrix  $D_{\text{DWF}}^{-1}$  (Eq. (3.2)):

$$\begin{aligned} D^{-1}(x, y) &= \langle q(x) \bar{q}(y) \rangle \\ &= \sum_{s, s'} \left( \frac{1 - \gamma_5}{2} \delta_{s, 0} + \frac{1 + \gamma_5}{2} \delta_{s, L_s - 1} \right) \langle \psi(x, s) \bar{\psi}(y, s') \rangle \left( \frac{1 + \gamma_5}{2} \delta_{s, 0} + \frac{1 - \gamma_5}{2} \delta_{s, L_s - 1} \right) \\ &= \sum_{s, s'} \left( \frac{1 - \gamma_5}{2} \delta_{s, 0} + \frac{1 + \gamma_5}{2} \delta_{s, L_s - 1} \right) D_{\text{DWF}}^{-1}(x, s; y, s') \left( \frac{1 + \gamma_5}{2} \delta_{s, 0} + \frac{1 - \gamma_5}{2} \delta_{s, L_s - 1} \right) \end{aligned} \quad (3.47)$$

$F(\vec{x}, \vec{y})$  is the smearing function which is defined in Eq.(3.14).

$c, c', c'', c'''$  are the color indices and  $\alpha, \alpha'$  are the spin indices. We apply the zero-momentum projection to obtain the meson mass from meson energy:  $E_{\vec{p}} = \sqrt{m_{\text{meson}}^2 + \vec{p}^2} \rightarrow m_{\text{meson}}$ , by summing over spatial volume  $\vec{x}, \vec{x}', \vec{y}, \vec{y}'$ . In eq. (3.41), the sum over  $\vec{y}$  is stochastically evaluated by the  $\mathbf{Z}_2$  noise source at  $t = 0$ , while the sums over  $\vec{x}$  and  $\vec{y}$  in (3.42) are evaluated by  $\mathbf{Z}_2$  source spreads over the space-time volume, *c.f.* (3.19) and (3.20):

$$\begin{aligned} & \frac{1}{N_{\text{noise}}} \sum_{n=1}^{N_{\text{noise}}} \sum_{\vec{x}, \vec{y}, \vec{z}} \langle \text{Tr}[\{G_{IJ}(\vec{x}, t; \vec{y}, 0) \xi^{(n)}(\vec{y}, 0)\} \Gamma \gamma_5 \{G_{IJ}(\vec{x}, t; \vec{z}, 0) \xi^{(n)}(\vec{z}, 0)\}^\dagger \gamma_5 \Gamma] \rangle \\ &= \frac{1}{N_{\text{noise}}} \sum_{n=1}^{N_{\text{noise}}} \sum_{\vec{x}, \vec{y}, \vec{z}} \langle \text{Tr}[G_{IJ}(\vec{x}, t; \vec{y}, 0) \Gamma \gamma_5 G_{IJ}^\dagger(\vec{x}, t; \vec{z}, 0) \gamma_5 \Gamma] \rangle \xi^{(n)}(\vec{y}, 0) \xi^{(n)*}(\vec{z}, 0) \\ &\rightarrow \sum_{\vec{x}, \vec{y}} \langle \text{Tr}[G_{IJ}(\vec{x}, t; \vec{y}, 0) \Gamma \gamma_5 G_{IJ}^\dagger(\vec{x}, t; \vec{y}, 0) \gamma_5 \Gamma] \rangle \quad (N_{\text{noise}} \rightarrow \infty), \\ &= \sum_{\vec{x}, \vec{y}} \langle \text{Tr}[G_{IJ}(\vec{x}, t; \vec{y}, 0) \Gamma G_{JI}(\vec{y}, 0; \vec{x}, t) \Gamma] \rangle, \end{aligned} \quad (3.48)$$

$$\begin{aligned} & \frac{1}{N_{\text{noise}}} \sum_{n=1}^{N_{\text{noise}}} \sum_{\vec{x}, \vec{y}, t'} \langle \text{Tr}[\xi^{(n)*}(\vec{x}, t) \{G_{II}(\vec{x}, t; \vec{y}, t') \xi^{(n)}(\vec{y}, t')\} \Gamma] \rangle \\ &\rightarrow \sum_{\vec{x}} \langle \text{Tr}[G_{II}(\vec{x}, t; \vec{x}, t) \Gamma] \rangle \quad (N_{\text{noise}} \rightarrow \infty), \end{aligned} \quad (3.49)$$

The dagger ( $\dagger$ ) is taken only for color and spinor (and not for space-time) indices, and we use the  $\gamma_5$  hermiticity,  $\gamma_5 D^{-1} \gamma_5 = [D^{-1}]^\dagger$ , of the propagator (3.47) in (3.48). The trace over color and spinor indices is exactly carried out by solving the quark propagator  $3 \times 4$  times each for a random source.

### 3.5. Meson mass fit

Throughout this paper, we assume that the one particle state is the ground state for quantum numbers  $I$  and  $J^{PC}$ , for compatibility with to the interpolation operator in Table II. This assumption is not entirely true for some cases. For example, a  $\rho$  meson may decay into pions. In our simulation, quarks are heavy with the lightest quark mass about half the strange quark mass, and confined in a relatively small ( $\sim 2$  fm)<sup>3</sup> box. Many of the decay processes would not occur in this setting since the decaying particles have energies above the threshold. Also we restrict ourselves to degenerate up and down quarks,  $N_f = 2$ , so that a meson such as  $a_0$  can not decay due to exact symmetry.

To extract the meson masses, the following two analyses are carried out.

#### (A) Standard method:

Only the ground state of mass  $m_O$  is assumed to exist in the correlation function  $\langle O_S O_S \rangle$ , which is fitted by the hyperbolic cosine function reflecting the periodic boundary condition for a meson at  $t = T$ ;

$$\sum_{\vec{x}, \vec{y}} \langle O_I(\vec{x}, t) O_I^\dagger(\vec{y}, 0) \rangle = \frac{V}{2m_O} |\langle 0 | O_I | O(\vec{p} = \vec{0}) \rangle|^2 [e^{-m_O t} + e^{-m_O(T-t)}], \quad (I = L, S) \quad (3.50)$$

for sufficiently large  $t$  and  $T - t$ . Although our main results will be obtained from the smeared-quark case,  $I = S$ , we also analyze local quark case to monitor the excited-state contamination. The fitting range of  $t$  is determined so that the effective meson mass becomes independent of the time. We also avoid a too large  $t$  for which the statistical error becomes large and the results become unreliable.

#### (B) Variational method:<sup>28), 29)</sup>

In this case, we also assume the first excited state of mass  $m_{O^*}$ . Both the local ( $I, J = L$ ) and the smeared ( $I, J = S$ ) interpolation fields are used to construct the correlation function  $\langle O_I O_J \rangle$ . The  $2 \times 2$  matrix,

$$X(t) = \begin{pmatrix} \sum_{\vec{x}, \vec{y}} \langle O_L(\vec{x}, t) O_L^\dagger(\vec{y}, 0) \rangle & \sum_{\vec{x}, \vec{y}} \langle O_L(\vec{x}, t) O_S^\dagger(\vec{y}, 0) \rangle \\ \sum_{\vec{x}, \vec{y}} \langle O_S(\vec{x}, t) O_L^\dagger(\vec{y}, 0) \rangle & \sum_{\vec{x}, \vec{y}} \langle O_S(\vec{x}, t) O_S^\dagger(\vec{y}, 0) \rangle \end{pmatrix}, \quad (3.51)$$

is normalized at a reference time  $t_0$  to reduce the statistical error, then is diagonalized

as

$$X^{-1/2}(t_0)X(t)X^{-1/2}(t_0) \xrightarrow{\text{diag.}} \begin{pmatrix} \lambda_O(t, t_0) & 0 \\ 0 & \lambda_{O^*}(t, t_0) \end{pmatrix}. \quad (3.52)$$

The eigenvalues are fit as a function of  $t$ ,

$$\lambda_O(t, t_0) = \frac{e^{-m_O t} + e^{-m_O(T-t)}}{e^{-m_O t_0} + e^{-m_O(T-t_0)}} \left( \overset{t, t_0 \ll T/2}{\rightarrow} e^{-m_O(t-t_0)} \right), \quad (3.53)$$

$$\lambda_{O^*}(t, t_0) = \frac{e^{-m_{O^*} t} + e^{-m_{O^*}(T-t)}}{e^{-m_{O^*} t_0} + e^{-m_{O^*}(T-t_0)}} \left( \overset{t, t_0 \ll T/2}{\rightarrow} e^{-m_{O^*}(t-t_0)} \right) \quad (3.54)$$

to obtain the masses of the states.

The second method, called the variational method, is employed to extract the ground-state energy precisely and to determine the amount of excited state contamination.

To fit  $\lambda(t, t_0)$  using eq. (3.53), without unknown amplitudes in front of the exponentials,  $t_0$  should be sufficiently large to ignore the higher excited states. By monitoring  $\lambda(t, t_0)$ , we verify, for our choice of  $t_0$ , that such contamination is not apparent within the current statistics. As an example  $a_0$  case is shown in Fig. 2.  $t_0 = 2$  (squares) is chosen for the final results as  $\lambda(t, t_0)$  for  $t_0 = 1$  (circles) can't be fit to a linear function of  $t - t_0$  meaning the meson propagator is not a single exponential, while those of  $t_0 > 2$  (diamonds, triangles) have much larger error bars. If the number of available configurations were larger, we would have observed the effect from the second excited state and should have calculated for more variations of interpolation field. This point may be important for future investigations with larger statistical sample.

For another example, the effective mass of  $a_0$ , which we will define in (4.1), obtained from the two methods is plotted in Fig. 3. The effective mass obtained from the variational method (squares) has the smallest statistical error, which is consistent with that of standard method using a smeared-smeared interpolation field (filled circles). For the variational method, the plateau appears after a smaller time distance when the excited-state is separated from the ground-state. The global fits to the plateaux are almost identical to each other. The clear signal of contamination from larger excited states for the local-local interpolation field (open circles) is observed. The identical central values and error bars from the standard single exponential fit and the variational method indicate that the effect from excited states is small for both methods with these settings.

We analyze all masses by both methods and compare the results to estimate the systematic uncertainty due to higher excited-states. We also explore the first excited state for pseudoscalar and vector mesons,  $\pi^*$  and  $\rho^*$ , using the variational method.

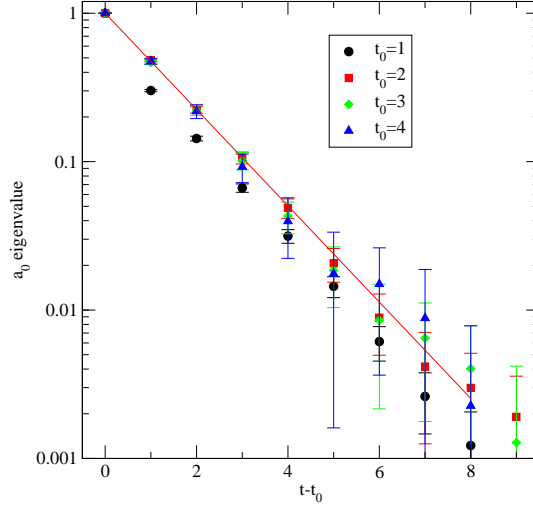


Fig. 2.  $t_0$  dependence of  $a_0$  eigenvalue for  $m_f = 0.02$ . We chose  $t_0 = 2$  (squares) by determining the contamination from the higher excited states.

### 3.6. Decay constant

The leptonic decay constant can be obtained from the amplitude of the two-point correlation function of a meson. We analyze decay constants for a pion,  $\pi^*$  and  $\rho$  mesons. Their respective decay constants,  $f_\pi$ ,  $f_{\pi^*}$  and  $f_\rho$  can be defined through the conserved axial and vector currents,  $\mathcal{A}_\mu^b(x)$  and  $\mathcal{V}_i^b(x)$ ,

$$f_O m_O = \langle 0 | \mathcal{A}_4^b(x) | O(\vec{p} = \vec{0}) \rangle = Z_A \langle 0 | A_4^b(x) | O(\vec{p} = \vec{0}) \rangle \quad (O = \pi, \pi^*) \quad (3.55)$$

$$f_\rho m_\rho \epsilon_i = \langle 0 | \mathcal{V}_i^b(x) | \rho(\vec{p} = \vec{0}) \rangle = Z_V \langle 0 | V_i^b(x) | \rho(\vec{p} = \vec{0}) \rangle \quad (i = 1, 2, 3) \quad (3.56)$$

where  $\epsilon_i$  is the polarization vector of the vector meson state, and  $Z_A$  and  $Z_V$  are the matching factors between the lattice local currents,

$$A_\mu^b(x) = \bar{q}(x) \tau^b \gamma_\mu \gamma_5 q(x), \quad (3.57)$$

$$V_\mu^b(x) = \bar{q}(x) \tau^b \gamma_\mu q(x), \quad (3.58)$$

and an appropriate renormalization is used scheme in the continuum QCD, which, in our case, is  $\overline{MS}$  at  $\mu = 2$  GeV.

For  $f_\pi$  and  $f_{\pi^*}$ , the first matrix element in (3.55) can be related to pseudoscalar density  $P^b(\vec{x}, t) = \bar{q}(x) \tau^b \gamma_5 q(x)$  using the (flavor nonsinglet) AWTI,

$$\partial_\mu \langle 0 | \mathcal{A}_\mu^b(x) O(0) | 0 \rangle = 2(m_f + m_{\text{res}}) \langle 0 | P^b(x) O(0) | 0 \rangle, \quad (3.59)$$

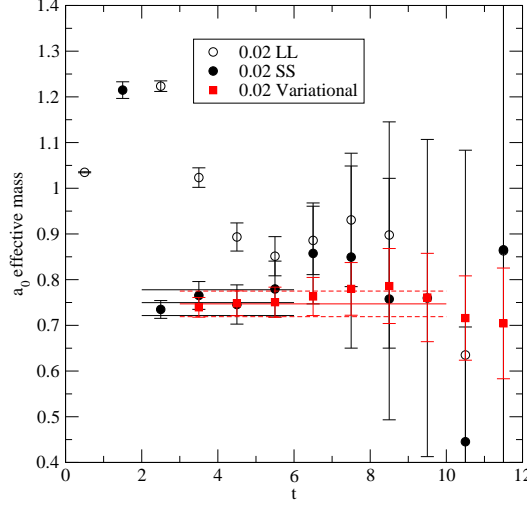


Fig. 3. Comparison of the effective mass of  $a_0$  obtained by the two methods. Open (filled) circles show the results from the local-local (smeared-smeared) interpolation field in the standard method while squares show the effective mass obtained in the variational method.

which leads to

$$f_O m_O^2 = 2(m_f + m_{\text{res}}) \langle 0 | P^b | O(\vec{p} = \vec{0}) \rangle \quad (O = \pi, \pi^*). \quad (3.60)$$

The actual determination of the decay constants is performed by the standard method (C) for a pion and  $\rho$  meson, and the variational method (D) for a pion and  $\pi^*$  meson:

(C) Standard method

In this case we assume the  $\langle \pi_L \pi_L \rangle$  and  $\langle \rho_L \rho_L \rangle$  correlation functions contain only propagation of the ground-state.  $\langle \pi_L \pi_L \rangle$  and  $\langle \rho_L \rho_L \rangle$  are fitted by a standard hyperbolic cosine function:

$$\begin{aligned} \sum_{\vec{x}, \vec{y}} \langle \pi_L(\vec{x}, t) \pi_L^\dagger(\vec{y}, 0) \rangle &= \frac{V}{2m_\pi} |\langle 0 | P_L^a | \pi(\vec{p} = \vec{0}) \rangle|^2 [e^{-m_\pi t} + e^{-m_\pi(T-t)}] \\ &= \frac{V f_\pi^2 m_\pi^3}{8(m_f + m_{\text{res}})^2} [e^{-m_\pi t} + e^{-m_\pi(T-t)}], \end{aligned} \quad (3.61)$$

$$\begin{aligned} \sum_{\vec{x}, \vec{y}} \langle \rho_L(\vec{x}, t) \rho_L^\dagger(\vec{y}, 0) \rangle &= \frac{V}{2m_\rho} |\langle 0 | V_L^a | \rho(\vec{p} = \vec{0}) \rangle|^2 [e^{-m_\rho t} + e^{-m_\rho(T-t)}] \\ &= \frac{V f_\rho^2 m_\rho}{2Z_V^2} [e^{-m_\rho t} + e^{-m_\rho(T-t)}], \end{aligned} \quad (3.62)$$

to extract the quantities  $m_\pi$ ,  $f_\pi$ ,  $m_\rho$ , and  $f_\rho/Z_V$ .



(D) Variational method

In this case, the second excited state,  $\pi^*$ , in the correlation function of the local meson operator,  $\langle \pi_L \pi_L \rangle$ , is also taken into account.  $\langle \pi_L \pi_L \rangle$  is fitted by a double hyperbolic cosine function:

$$\begin{aligned} \sum_{\vec{x}, \vec{y}} \langle \pi_L(\vec{x}, t) \pi_L^\dagger(\vec{y}, 0) \rangle &= \frac{V}{2m_\pi} |\langle 0 | P_L^a | \pi(\vec{p} = \vec{0}) \rangle|^2 [e^{-m_\pi t} + e^{-m_\pi(T-t)}] \\ &\quad + \frac{V}{2m_{\pi^*}} |\langle 0 | P_L^a | \pi^*(\vec{p} = \vec{0}) \rangle|^2 [e^{-m_{\pi^*} t} + e^{-m_{\pi^*}(T-t)}] \\ &= \frac{V f_\pi^2 m_\pi^3}{8(m_f + m_{\text{res}})^2} [e^{-m_\pi t} + e^{-m_\pi(T-t)}] + \frac{V f_{\pi^*}^2 m_{\pi^*}^3}{8(m_f + m_{\text{res}})^2} [e^{-m_{\pi^*} t} + e^{-m_{\pi^*}(T-t)}]. \end{aligned} \quad (3.63)$$

In this fitting procedure, we first determine  $m_\pi$  and  $m_{\pi^*}$  by the variational method, (B) in the previous subsection and then fit the two-point function data to (3.63) to determine  $f_\pi$  and  $f_{\pi^*}$  using the results from the first fitting.

### 3.7. Chiral Extrapolation

To obtain the masses and decay constants of various mesons at the physical quark mass point,  $m_f = m_{u,d}$ ,<sup>25)</sup> we need to extrapolate the numerical value calculated at heavier quark mass points. As the number of simulation points is limited and the statistical error is too large, we do not use the fitting formula of chiral perturbation theory at the next leading order or higher in this work.

As a crude estimation of the mass of  $\eta'$  at the physical point, we examine the formula valid in the lowest-order approximation from the flavor singlet AWTI given by eq. (3.59):

$$m_{\eta'}^2 = C_0 + C_1(m_f + m_{\text{res}}) \quad (\text{AWTI type}), \quad (3.64)$$

We also examine the simplest linear extrapolation for all meson masses as well as the decay constants,

$$O = C_0 + C_1(m_f + m_{\text{res}}) \quad (\text{linear type}) \quad (3.65)$$

where  $O$  is either a meson mass or a decay constant.

## §4. Numerical results

### 4.1. Mass of $\rho$ meson and lattice scale

First we analyze the mass of a  $\rho$  meson using the methods (A) and (B) and determine the lattice scale from  $m_\rho$  assuming that it is a stable particle, which is true for the relatively heavy quark in the small box used in our simulation. In Fig. 4, the effective mass of a  $\rho$  meson

Table III.  $m_\rho$ 

$m_f$	$m_\rho$	$t_0$	$t_{\min}$	$t_{\max}$	method
0.02	0.5741(39)		5	11	(A)
	0.5729(41)	5	$t_0 + 1$	12	(B)
	0.5425(64) <sup>a</sup>		5	16	(A)
0.03	0.5979(40)		7	14	(A)
	0.5984(34)	5	$t_0 + 1$	16	(B)
	0.5946(58) <sup>a</sup>		6	16	(A)
0.04	0.6385(39)		6	14	(A)
	0.6379(35)	5	$t_0 + 1$	16	(B)
	0.6323(70) <sup>a</sup>		7	16	(A)

<sup>(a)</sup> These values are obtained from  $(I, J) = (L, W)$  correlation functions and quoted by.<sup>25)</sup>

meson, taken from the damping rate between meson propagators at two neighboring times,  $m_{\rho, IJ}^{\text{eff}}(t + 1/2)$ , which is defined as

$$\frac{\sum_{\vec{x}, \vec{y}} \langle O_I(\vec{x}, t) O_J^\dagger(\vec{y}, 0) \rangle}{\sum_{\vec{x}, \vec{y}} \langle O_I(\vec{x}, t + 1) O_J^\dagger(\vec{y}, 0) \rangle} = \frac{e^{-m_{O, IJ}^{\text{eff}}(t + \frac{1}{2})} t + e^{-m_{O, IJ}^{\text{eff}}(t + \frac{1}{2})} (T - t)}{e^{-m_{O, IJ}^{\text{eff}}(t + \frac{1}{2})} (t + 1) + e^{-m_{O, IJ}^{\text{eff}}(t + \frac{1}{2})} (T - t - 1)} , \quad (4.1)$$

is plotted in the top panels (method (A) and method (B) are shown in the left and right panels, respectively). The bottom panel shows an eigenvalue of the ground-state obtained from the variational method. The results of  $m_\rho$  obtained from the standard hyperbolic cosine fit (method (A)) and the variational method (method (B)) are listed in Table III. The masses obtained from both methods are consistent with each other within statistical error for all  $m_f$ , and the ground-state mass can be successfully extracted using the smeared operator.

We perform linear extrapolation for both results and obtain  $m_\rho$  at the physical quark mass point ( $m_f = m_{u,d}$ ). The result of the chiral extrapolation is shown in Fig. 5 and Table IV. The values obtained from both methods at the physical quark mass point are consistent within statistical error; we choose the value from method (B) as our main value. The lattice scale determined from  $m_\rho = 775.49 \text{ MeV}^{1)}$  is

$$a_{m_\rho}^{-1} = 1.537(26) \text{ GeV} . \quad (4.2)$$

We have measured the potential energy between static quarks and extracted the Sommer scale  $r_0$  from the potential  $r_0/a = 4.278(54)$ .<sup>25)</sup> Using  $a_{m_\rho}$  we obtained

$$r_0^{\text{phys}} = 0.5491(93) \text{ fm} , \quad (4.3)$$

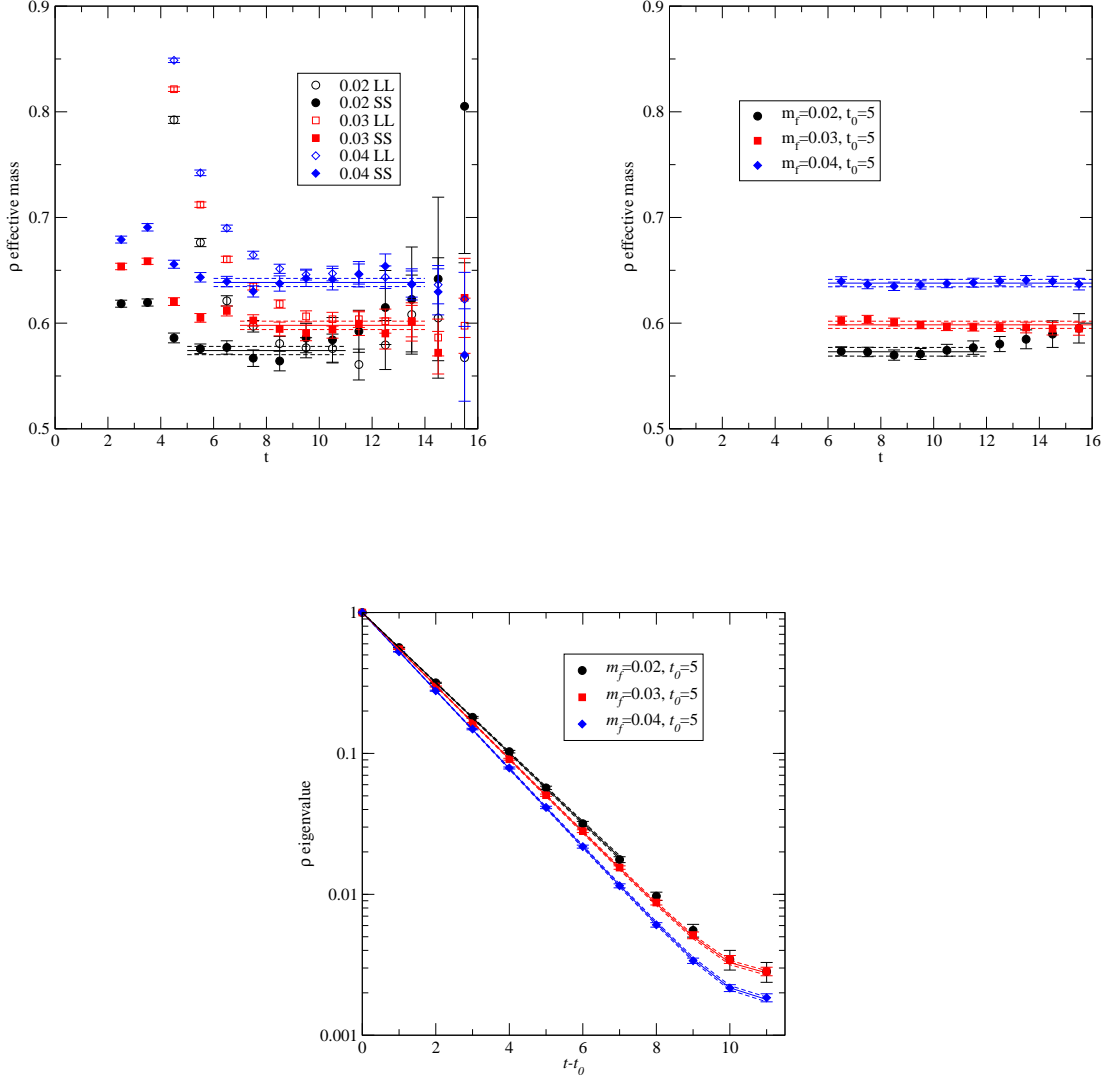


Fig. 4. Effective mass of  $\rho$  vs  $t$  using method (A) (left) and method (B) (right), and  $\rho$  eigenvalue vs  $t - t_0$  (bottom). Lines show the globally fitted result with errors and the ranges of  $t$ .

which is somewhat larger than previously estimated values by  $\sim 10\%$ . Although  $r_0$  is one of the most precisely determined dimensionful quantities in the lattice QCD, its experimental value is not known; thus, we could not judge whether our larger value is close to the physical value in QCD or whether it reflects some systematic errors, which we discuss in a later section.

By increasing the statistical sample size, the lattice scale changed from that we reported in our previous paper.<sup>25)</sup> Accordingly, the physical quark mass point,  $m_f = m_{u,d}$ , may

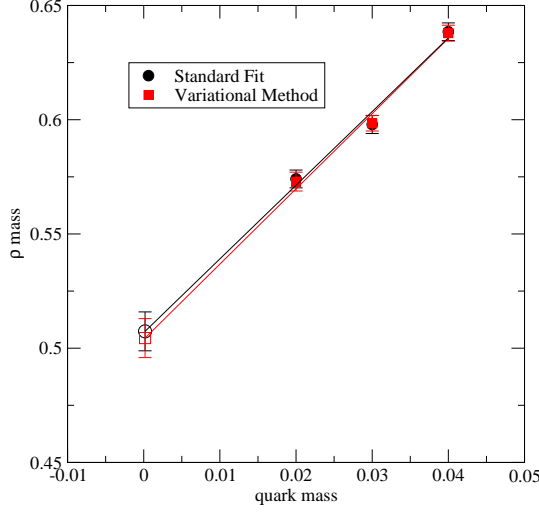


Fig. 5.  $m_\rho$  vs  $m_f$

Table IV.  $m_\rho$  at the physical quark mass point ( $m_f = m_{u,d}$ ).

$m_\rho$	$a_{m_\rho}^{-1}$ [GeV]	$a_{m_\rho}$ [fm]	method
0.5073(85)	1.528(26)	0.1291(22)	(A)
0.5044(85)	1.537(26)	0.1284(22)	(B)

change. However, we use the old value of  $m_{u,d}$  as the physical quark mass point in this paper. This is because the number of quark mass points newly obtained in this work is not sufficient to repeat the same analysis as before in which we used the formula of ChPT up to the next to the leading order. We will discuss the decay constant and the excited-state meson,  $\rho^*$ , in later sections.

#### 4.2. Pion mass

In Fig. 6, we plot the effective mass of a pseudoscalar meson obtained by method (A) on the left, that obtained by method (B) on the right, and the ground-state eigenvalue obtained using method (B) on the bottom panel. Table V summarizes the values of the pion mass obtained by both methods. By using 5-10 times more statical samples than in the previous analysis and extracting the ground-state information from the meson propagator over shorter time distance, which becomes possible using smeared operators, the statistical errors decrease to approximately half of those in the previous results. The fact that the reduction of the error size is closer to or even larger than that expected from the increase

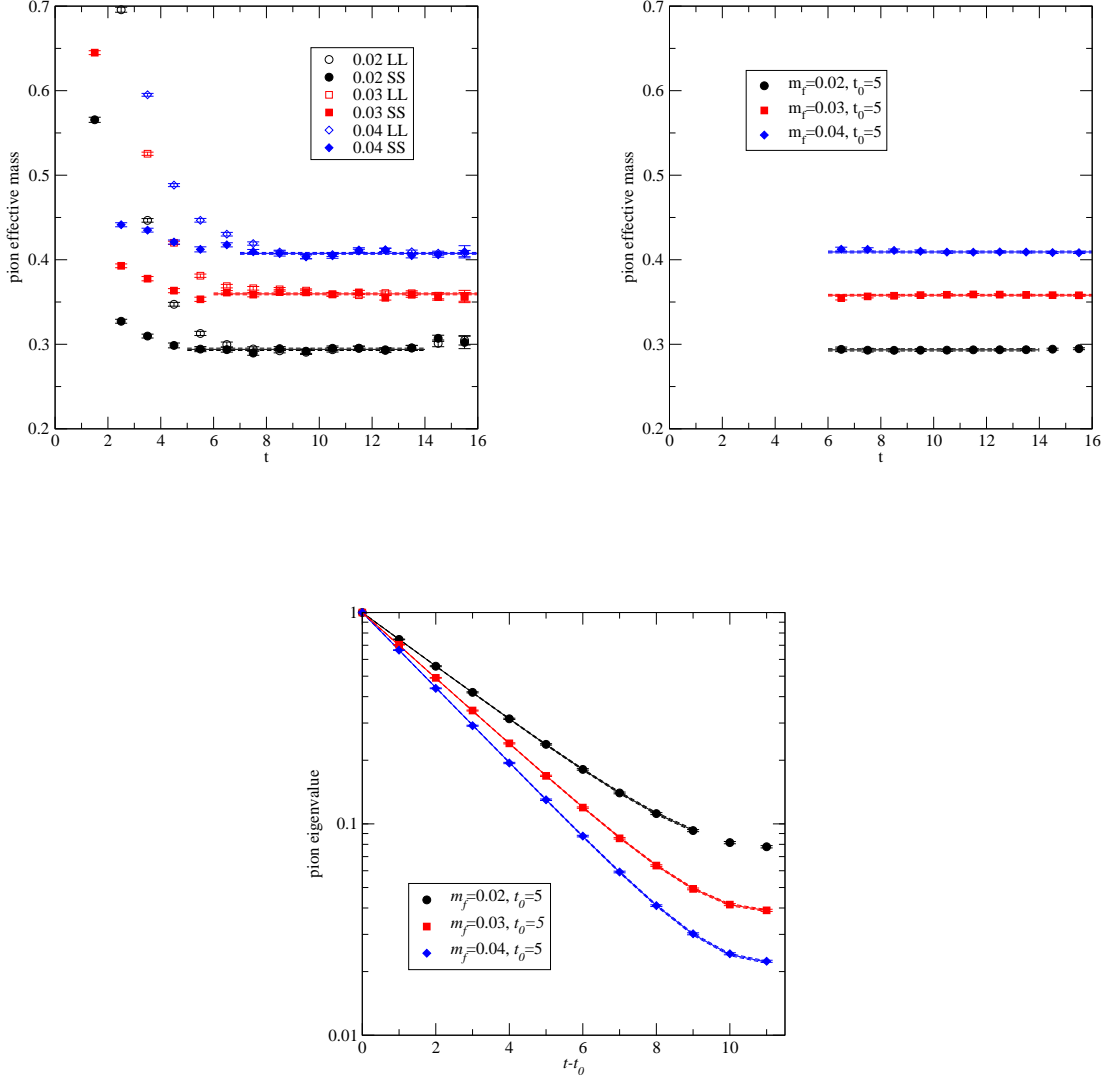


Fig. 6. Pion effective mass vs.  $t$  using method (A) (left) and method (B) (right), and pion eigenvalue vs.  $t - t_0$  (bottom). Lines show fit values, errors and ranges.

in the number of statistical samples,  $1/2 > 1/\sqrt{5-10}$ , suggests that the smearing itself does not necessarily cause the smaller statistical error for a pseudoscalar meson. Rather, we could determine the extent of the excited-state contamination using smeared operators with different overlaps with the states. In fact, our new results are consistent within statistical error with the previous results. We will discuss the decay constant and the excited-state meson,  $\pi^*$ , later.

Table V.  $m_\pi$ 

$m_f$	$m_\pi$	$t_0$	$t_{\min}$	$t_{\max}$	method
0.02	0.2940(14)		5	14	(A)
	0.2934(13)	5	$t_0 + 1$	14	(B)
	0.2902(28) <sup>a</sup>		9	16	(A)
0.03	0.3596(11)		6	16	(A)
	0.3581(10)	5	$t_0 + 1$	16	(B)
	0.3575(19) <sup>a</sup>		9	16	(A)
0.04	0.4075(11)		7	16	(A)
	0.4092(11)	5	$t_0 + 1$	16	(B)
	0.4094(25) <sup>a</sup>		9	16	(A)

<sup>(a)</sup> These values are obtained from  $(I, J) = (L, W)$  correlators and quoted by.<sup>25)</sup>

#### 4.3. Mass of $a_0$

From experiments, there are two flavor-non-singlet scalar mesons,  $a_0(980)$  and  $a_0(1450)$ , in nature. Although these are unstable particles in the more realistic  $N_f = 2 + 1$  case, we assume a stable one-particle state to be the ground state in the scalar meson sector in our  $N_f = 2$  case with a relatively heavy quark and small space-time.  $a_0$  meson spectrum results previously obtained by lattice QCD calculation seem to fall roughly into two categories,<sup>43)</sup> studies reporting lighter masses of  $\sim 1$  GeV<sup>42), 44)</sup> and those reporting heavier masses  $\sim 1.5$  GeV.<sup>26), 43), 45), 46)</sup> Previous RBC results<sup>26)</sup> are  $m_{a_0} = 1.58(34)$  GeV by the analysis of unitary points and 1.51 (19) GeV by partially quenched analysis.

Fig. 7 (left) shows the effective mass of  $a_0$ , Fig. 7 (right) shows the eigenvalue of the ground-state using the variational method (B). The numerical values are listed in Table VI, in which we also quote the previous RBC values.<sup>26)</sup>

Our new results for the mass of  $a_0$  are significantly lighter than those of previous results, as shown in Table VI. Since the QCD ensemble used in both investigations is the same, this discrepancy must originate from the difference in measuring the meson operator. In the previous calculation the meson interpolation field was constructed from quark fields at a point. Although the point operator was convenient for theoretical investigation in the previous study, it is not necessarily optimal for extracting the ground state. In fact, as shown in the left panel of Fig. 7, the effective mass of the point operator (open symbols) is very large at a short distance, which implies a large amount of excited-state contamination in the point operator. On the other hand, the effective mass obtained using the smeared operator (filled symbols) reaches plateaux earlier in time and coincides to that obtained from

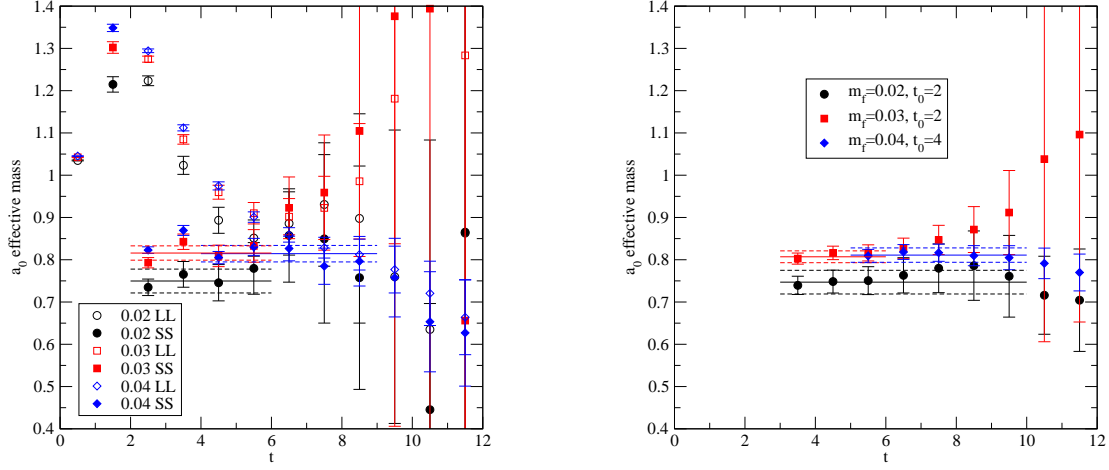


Fig. 7. Effective mass of  $a_0$  vs  $t$  using method (A) (left) and method (B) (right). Lines show fitted values, errors, and ranges.

Table VI.  $m_{a_0}$

$m_f$	$m_{a_0}$	$t_0$	$t_{\min}$	$t_{\max}$	method
0.02	0.750(28) <sup>a</sup>		2	6	(A)
	0.747(28)	2	$t_0 + 1$	10	(B)
	0.92(9) <sup>b</sup>		4	10	exponential fit
0.03	0.816(17) <sup>a</sup>		2	6	(A)
	0.807(14)	2	$t_0 + 1$	6	(B)
	0.99(10) <sup>b</sup>		5	10	exponential fit
0.04	0.814(19) <sup>a</sup>		4	9	(A)
	0.811(17)	4	$t_0 + 1$	10	(B)
	0.94(5) <sup>b</sup>		5	12	exponential fit

<sup>(a)</sup> These values are obtained by uncorrelated fitting. <sup>(b)</sup> These values are obtained from  $(I, J) = (L, L)$  correlators and quoted in 26).

the ground-state eigenvalue by the variational method, shown in right panel. Note that the size of the statistical sample is increased by a factor of five or more in this work compared with that in the previous report.

Fig. 8 shows the results of extrapolation by linear fitting and Table VII shows  $m_{a_0}$  at the physical quark mass point. Since both methods (A) and (B) are consistent with each

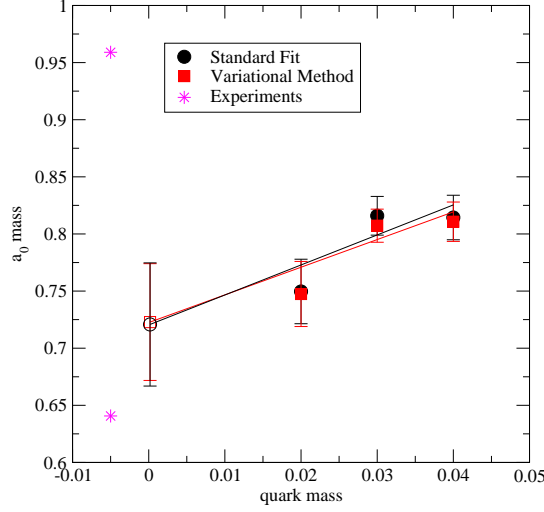


Fig. 8.  $m_{a_0}$  vs  $m_f$ . The asterisk on the left shows the experimental values.<sup>1)</sup>

Table VII.  $m_{a_0}$  at the physical quark mass point ( $m_f = m_{u,d}$ ).

$m_{a_0}$	$m_{a_0}^{\text{phys}}$ [MeV]	$m_{a_0} r_0$	method
0.721(54)	1,108(85)	3.08(23)	(A)
0.723(51)	1,111(81)	3.10(22)	(B)

other we choose

$$m_{a_0}^{\text{phys}} = 1.111(81) \text{ GeV} \quad (4.4)$$

from method (B) as our final value in this work.

To clarify the discrepancies among results obtained from lattice calculations and experiments, further investigations including the calculation multiparticle scattering states and the strange sea quark effects ( $N_f = 2 + 1$ ) are needed.

#### 4.4. Mass of $\eta'$

Before presenting the mass spectrum results of the flavor singlet pseudoscalar meson,  $\eta'$ , we check whether the theoretical expectation discussed in §2 is realized. The ratio of the correlation function between disconnected quark loops,  $D_{\gamma_5}(t)$ , to the connected correlation function,  $C_{\gamma_5}(t)$ , was shown to approach unity for a large time separation, which is clearly different from the expectation of the linear growth in the quenched QCD case (2.9). In the discussion, only the pion and  $\eta'$  states were considered when coupling to the  $I(J^P) = 0(0^-)$



operator, leading to

$$\frac{N_f D_{\gamma_5}(t)}{C_{\gamma_5}(t)} = 1 - B \frac{e^{-m_{\eta'} t} + e^{-m_{\eta'}(T-t)}}{e^{-m_{\pi} t} + e^{-m_{\pi}(T-t)}} \xrightarrow{(T-t) \gg 1} 1 - B e^{-(m_{\eta'} - m_{\pi})t}. \quad (4.5)$$

In Fig. 9, the ratio extracted using the smeared operator,  $\eta'_S$ , is plotted. Indeed the ratio asymptotically approaches one for the two lighter quark masses (circles, squares), although it is statistically uncertain at a large time distance. However the heaviest quark mass point (diamonds) seems to approach to a value lower than one. The mass difference between  $\eta'$  and  $\pi$  is smaller for the heavier quark mass, and is close to zero for the heaviest quark mass (as we will discuss later); thus, the ratio only approaches unity at a very large  $t$  from (2.6). Moreover, this deviation from the simplest theoretical explanation might be due to the omission of the excited states such as the  $\pi^*$  or  $0^{-+}$  glueball state, which may play a more significant role in the heavier-quark-mass region. From the current results, we can not conclude whether the deviation from unity for the heaviest quark can be explained by the above-mentioned arguments or is due to other reasons, for example, insufficient sampling of the different topological sectors.

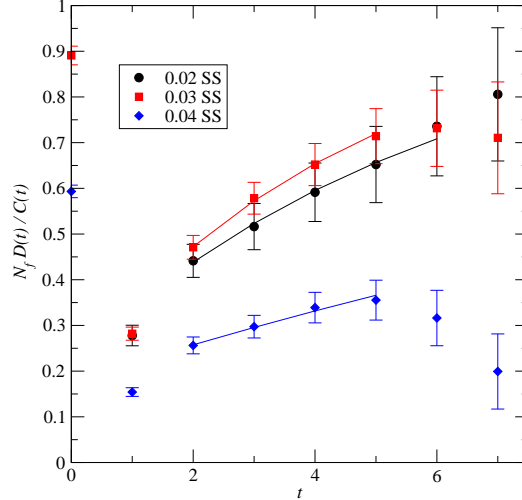


Fig. 9.  $N_f D_{\gamma_5}(t)/C_{\gamma_5}(t)$  vs  $t$ .

We now describe the  $\eta'$  spectrum obtained using methods (A) and (B). Figure 10 shows the effective mass (left: method (A), right: method (B)), and the ground-state eigenvalue, and their numerical values and their fitted ranges are given in Table VIII. We did not use a propagator from longer distance, where the statistics are too poor and the standard error

Table VIII.  $m_{\eta'}$ .

$m_f$	$m_{\eta'}$	$t_0$	$t_{\min}$	$t_{\max}$	method
0.02	0.477(40)		2	5	(A)
	0.473(50)	2	$t_0 + 1$	6	(B)
0.03	0.571(60)		3	5	(A)
	0.600(44)	2	$t_0 + 1$	6	(B)
0.04	0.497(17)		2	5	(A)
	0.492(15)	2	$t_0 + 1$	5	(B)

analysis would not be reliable, although the inclusion of a few more data points does not change the fitted results for most of the masses. Method (B) produces flatter plateaux than method (A) for this meson.

As a consistency check, we also examined the temporal exponent of the ratio (2.6) to extract the mass of  $\eta'$ . We have evaluated the effect of the finiteness of the lattice in the temporal direction by using the fitting formula (2.5), and found the results to be unchanged. Combining the measured pion mass in Table V, the values obtained are  $m_{\eta'} = 0.458(58)$ ,  $0.571(48)$ , and  $0.461(15)$  for  $m_f = 0.02$ ,  $0.03$ , and  $0.04$ , respectively. These estimations are slightly smaller than the results in Table VIII. One reason for this may be that the time range used in fitting the ratio is too short and the pion mass is overestimated, which causes the estimation for the mass of  $\eta'$  to be smaller than its actual value. Because of this possibility, we won't use the results obtained from the ratio fitting in our main results.

The mass of  $\eta'$  has only slight dependence on the quark mass, as shown in Fig. 11: all three masses are consistent within two to three standard deviations of statistical error. Their central value fluctuates nonmonotonically in quark mass order. Before being convinced of this nonmonotonicity, we should question the reliability of the error estimation and other systematic uncertainties such as insufficient sampling over the topological charge since  $\eta'$  is likely to depend strongly on the topological charge. In our simulation we use DBW2 gauge action to reduce the size of the residual chiral symmetry breaking,  $m_{\text{res}}$ , sacrificing the configuration mobility among different topological sectors to some extent.

Although the quark mass dependence has not been resolved sufficiently clearly, we extrapolate the measured masses by the eqs. (3.64) and (3.65) to estimate the mass of  $\eta'$  at the physical quark mass point. The results are shown in Fig. 11 and Table IX. The central values of the estimation differ from each other by 15% but are within statistical error. Our main estimation for the mass of  $\eta'$  at the physical quark mass point is obtained from the variational method (B) and chiral extrapolation using the lowest order of ChPT (3.64), and

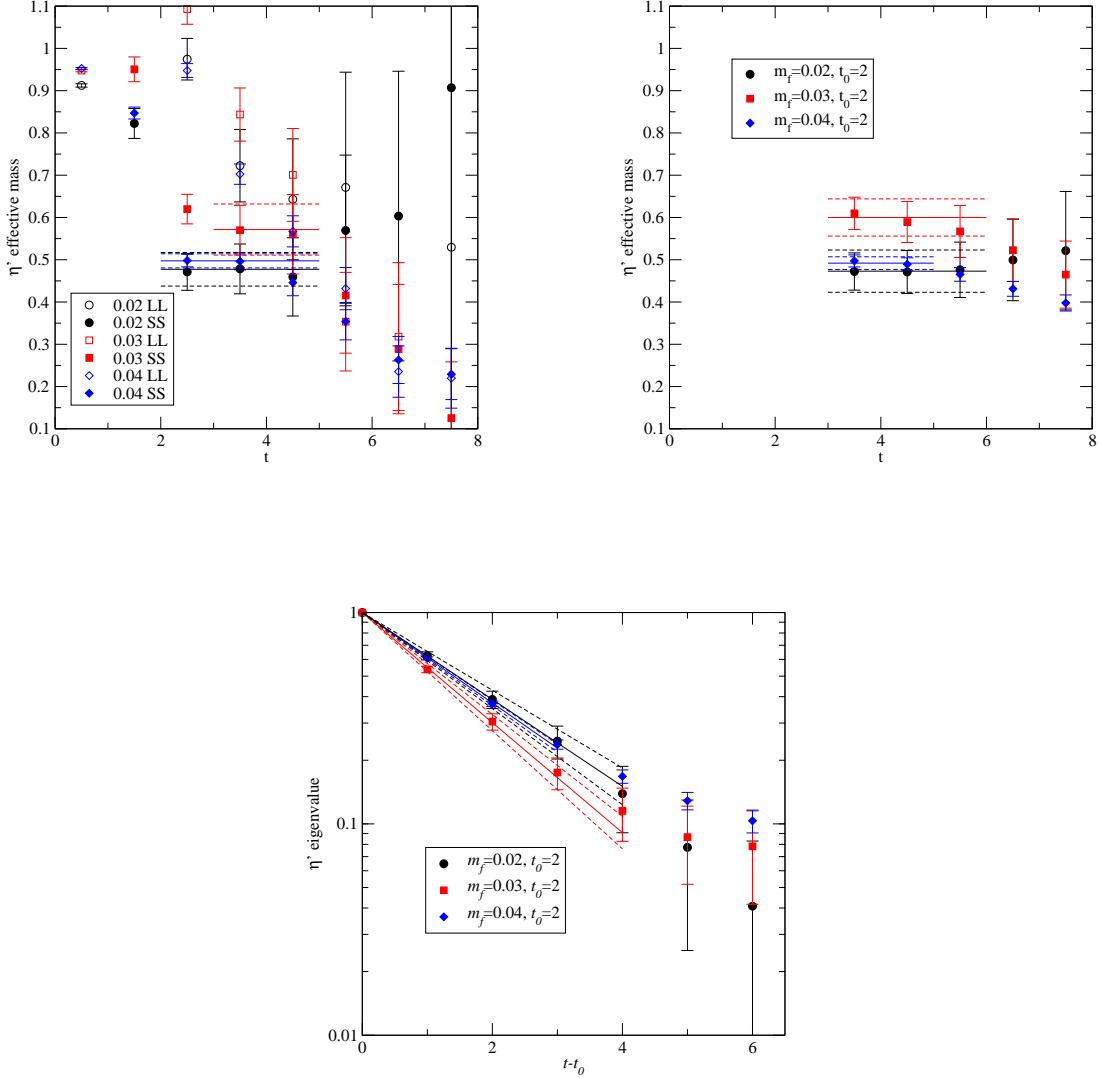


Fig. 10. Effective mass of  $\eta'$  vs  $t$  using method (A) (left) and method (B) (right), and  $\eta'$  eigenvalue vs  $t - t_0$  (bottom).

is given by

$$m_{\eta'}^{\text{phys}} = 819(127) \text{ MeV} . \quad (4.6)$$

This is the first estimation of the mass of  $\eta'$  performed with the two flavors of a dynamical (approximately) chiral fermion, which is certainly heavier than a pion, which is thought to be related to the chiral  $U(1)_A$  anomaly. Apart from the large statistical error and the various systematic errors discussed above, the main results are close to the experimentally obtained

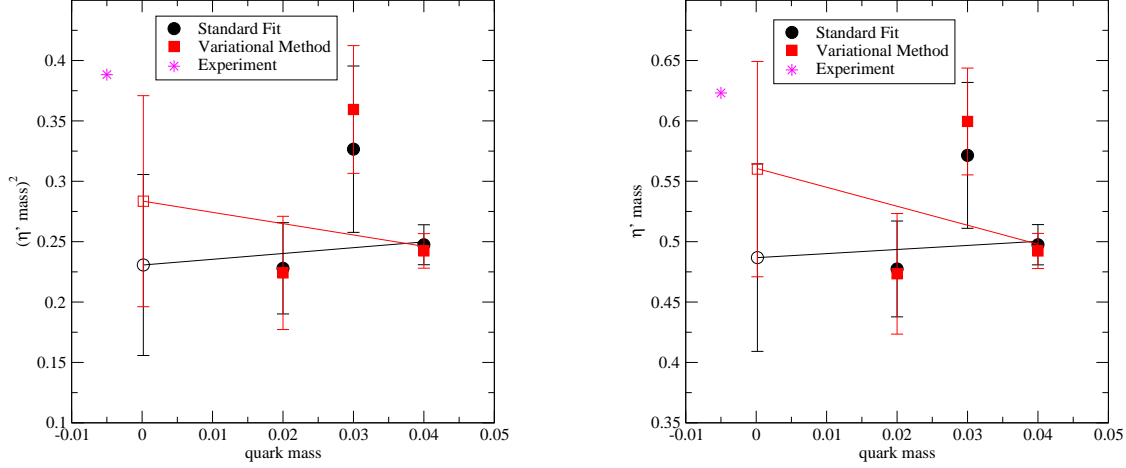


Fig. 11.  $m_{\eta'}^2$  vs  $m_f$  (left), and  $m_{\eta'}$  vs  $m_f$  (right). The open circles and squares are extrapolated values at the physical quark mass point using (3.64) and (3.65), respectively. The asterisk on the left shows the experimental values.<sup>1)</sup>

Table IX.  $m_{\eta'}$  at the physical quark mass point ( $m_f = m_{u,d}$ ).

$m_{\eta'}$	$m_{\eta'}^{\text{phys}}$ [MeV]	$m_{\eta'} r_0$	method and chiral extrapolation
0.480(78)	738(121)	2.05(33)	(A) AWTI type (3.64)
0.487(78)	748(120)	2.08(33)	(A) linear type (3.65)
0.532(82)	819(127)	2.28(35)	(B) AWTI type (3.64)
0.560(89)	862(130)	2.40(36)	(B) linear type (3.65)

mass of  $\eta'$ , which suggests that further improvements can be made by especially calculation using an  $N_f = 2 + 1$  ensemble.

#### 4.5. Mass of $\omega$

We also examine the flavor singlet vector meson,  $\omega$ , using a similar procedure to that for  $\eta'$ . Fig. 12 shows the effective mass of  $\omega$  (left: method (A), right: method (B)), which is also listed in Table X. We are able to extract a non-zero signal, but from a shorter time distance; thus there may be a significant distortion from the excited states. The results for the lightest point,  $m_f = 0.02$ , has a particularly poor signal.

We estimated the extrapolated mass at the physical quark mass point, as shown in Fig. 13 and Table XI. The fitting formula used is the linear extrapolation (3.65). Since the statistical error for the lightest point  $m_f = 0.02$  is large, as mentioned above, we examine two ways of

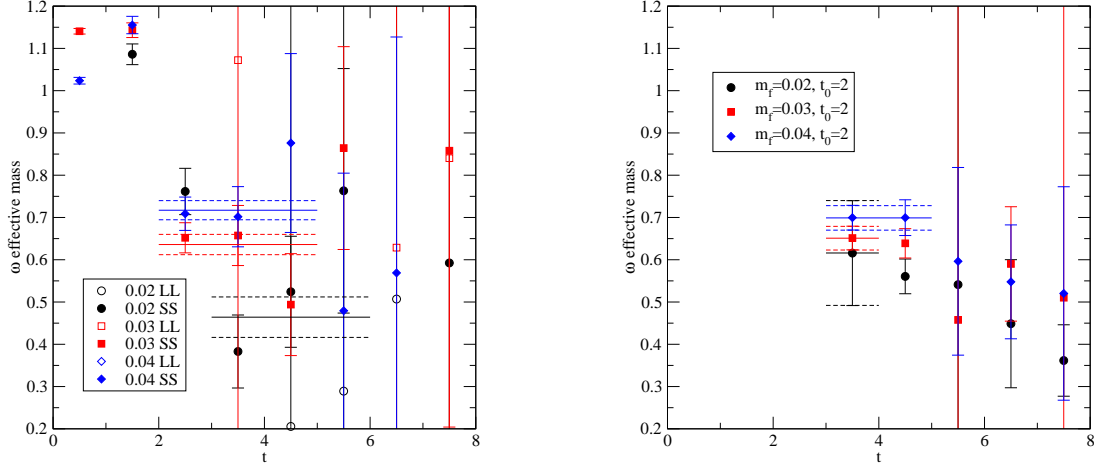


Fig. 12. Effective mass of  $\omega$  vs  $t$  using method (A) (left) and method (B) (right).

Table X.  $m_\omega$ .

$m_f$	$m_\omega$	$t_0$	$t_{\min}$	$t_{\max}$	method
0.02	0.464(48)		3	6	(A)
	0.616(124)	2	$t_0 + 1$	4	(B)
0.03	0.636(24)		2	5	(A)
	0.651(28)	2	$t_0 + 1$	4	(B)
0.04	0.717(23)		2	5	(A)
	0.699(29)	2	$t_0 + 1$	5	(B)

the chiral extrapolation: using all three masses or the heaviest two points. In Table XI, one can see that the results obtained from the “method (A) 3-masses fitting” are significantly different from those of the “method (A) 2-masses fitting”. At the physical quark mass point,  $m_\omega$  is obtained from the “method (B) 3 masses fitting”,

$$m_\omega^{\text{phys}} = 790(194) \text{ MeV} . \quad (4.7)$$

Our estimation for  $\omega$  is consistent with the experimental value, but with a large statistical error  $\sim 25\%$ .

We also calculated the propagators of the flavor singlet meson scalar,  $f_0$ , using the same quark propagator for  $\eta'$  and  $\omega$ , and found that they are too noisy to extract the spectrum for all values of  $m_f$ .

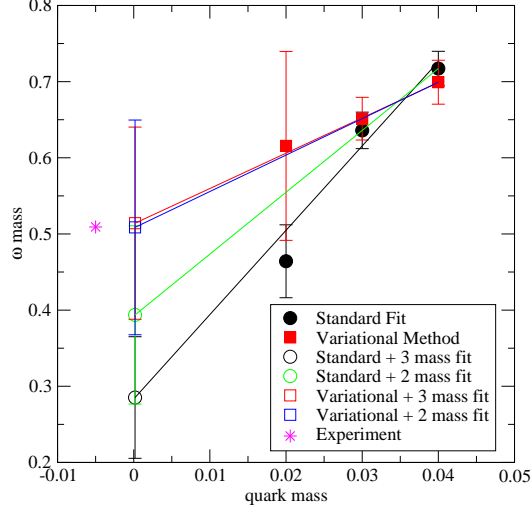


Fig. 13.  $m_\omega$  vs  $m_f$ . The asterisk on the left shows the experimental value.<sup>1)</sup>

Table XI. Estimation of  $m_\omega$  at the physical quark mass point ( $m_f = m_{u,d}$ ).

$m_\omega$	$m_\omega^{\text{phys}}$ [MeV]	$m_\omega r_0$	fit method
0.285(80)	439(123)	1.22(34)	(A) 3 masses fit
0.394(117)	605(180)	1.68(50)	(A) 2 masses fit
0.514(126)	790(194)	2.20(54)	(B) 3 masses fit
0.509(141)	782(217)	2.18(60)	(B) 2 masses fit

#### 4.6. Pseudovector meson ( $a_1$ , $b_1$ , $f_1$ , $h_1$ ) spectra

Figs. 14, 15, 16, and 17 show the effective mass obtained using method (A) (left) and method (B) (right), and Tables XII, XIII-XV list the results of fits for  $a_1$ ,  $b_1$ ,  $f_1$ , and  $h_1$ , respectively. Except for the  $h_1$  meson propagator at  $m_f = 0.03$ , the fitting procedure converges.

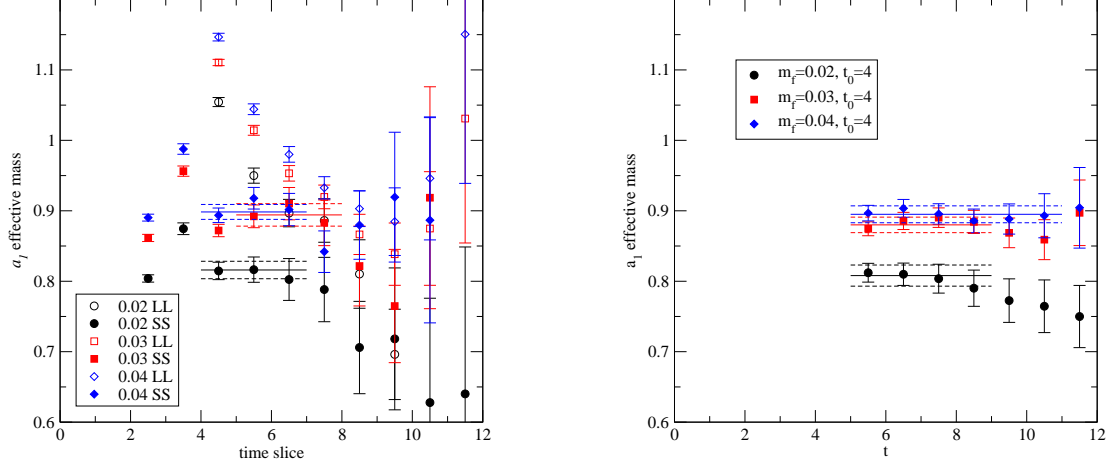


Fig. 14. Effective mass of  $a_1$  vs  $t$  using method (A) (left) and method (B) (right).

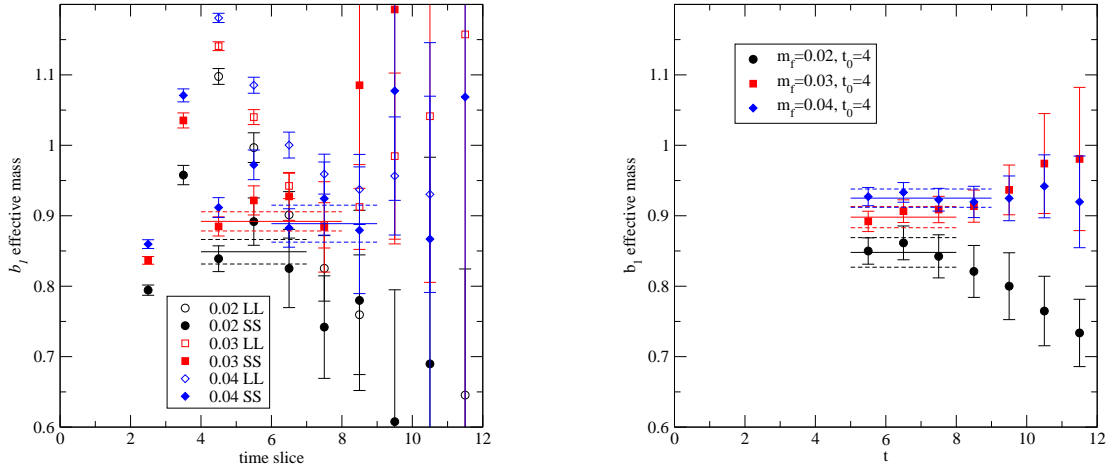


Fig. 15. Effective mass of  $b_1$  vs  $t$  using method (A) (left) and method (B) (right).

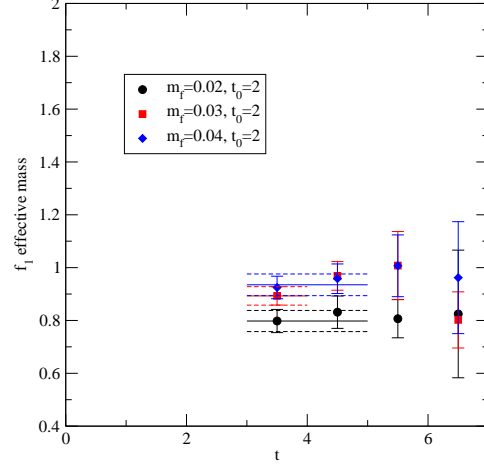
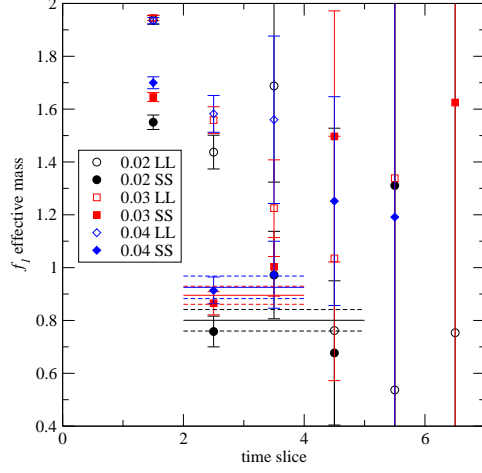


Fig. 16. Effective mass of  $f_1$  vs  $t$  using method (A) (left) and method (B) (right).

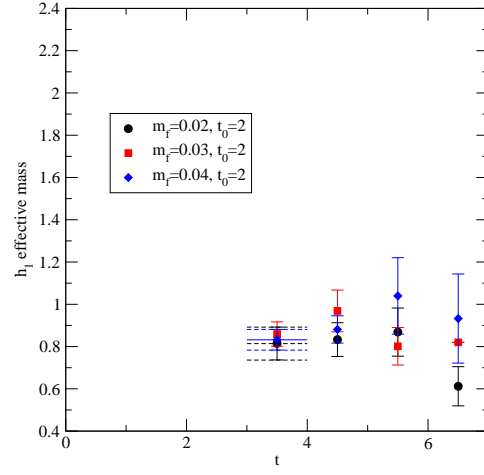
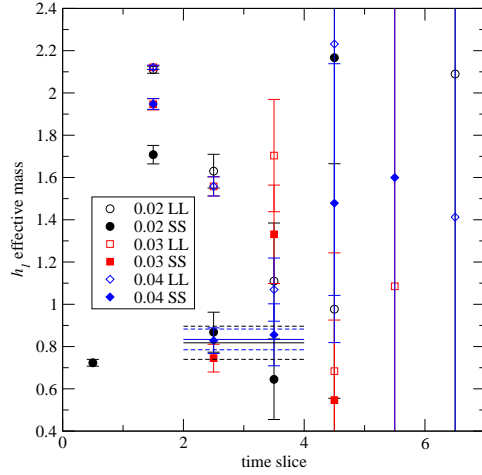


Fig. 17. Effective mass of  $h_1$  vs  $t$  using method (A) (left) and method (B) (right).



Table XII.  $m_{a_1}$ .

$m_f$	$m_{a_1}$	$t_0$	$t_{\min}$	$t_{\max}$	method
0.02	0.816(12)		4	7	(A)
	0.808(15)	4	$t_0 + 1$	9	(B)
0.03	0.894(16)		5	8	(A)
	0.880(11)	4	$t_0 + 1$	9	(B)
0.04	0.898(11)		4	8	(A)
	0.895(12)	4	$t_0 + 1$	11	(B)

Table XIII.  $m_{b_1}$ .

$m_f$	$m_{b_1}$	$t_0$	$t_{\min}$	$t_{\max}$	method
0.02	0.849(17)		4	7	(A)
	0.848(21)	4	$t_0 + 1$	8	(B)
0.03	0.892(14)		4	8	(A)
	0.898(15)	4	$t_0 + 1$	8	(B)
0.04	0.889(26)		6	9	(A)
	0.925(13)	4	$t_0 + 1$	9	(B)

Table XIV.  $m_{f_1}$ .

$m_f$	$m_{f_1}$	$t_0$	$t_{\min}$	$t_{\max}$	method
0.02	0.801(41)		2	5	(A)
	0.798(40)	2	$t_0 + 1$	5	(B)
0.03	0.895(34)		2	4	(A)
	0.893(35)	2	$t_0 + 1$	4	(B)
0.04	0.925(43)		2	4	(A)
	0.935(41)	2	$t_0 + 1$	5	(B)

These meson masses are extrapolated linearly to the physical quark mass point,  $m_f = m_{u,d}$ , and are shown in Figs. 18-21. The numerical values are summarized in Tables XVI-XIX for  $a_1$ ,  $b_1$ ,  $f_1$ , and  $h_1$ , respectively. As the masses are independent of the method used, within statistical error, we choose

$$m_{a_1}^{\text{phys}} = 1.140(51) \text{ GeV} , \quad (4.8)$$

$$m_{b_1}^{\text{phys}} = 1.203(64) \text{ GeV} , \quad (4.9)$$

$$m_{f_1}^{\text{phys}} = 1.033(137) \text{ GeV} , \quad (4.10)$$

Table XV.  $m_{h_1}$ .

$m_f$	$m_{h_1}$	$t_0$	$t_{\min}$	$t_{\max}$	method
0.02	0.818(78)		2	4	(A)
	0.814(78)	2	$t_0 + 1$	4	(B)
0.04	0.834(49)		2	4	(A)
	0.832(49)	2	$t_0 + 1$	4	(B)

$$m_{h_1}^{\text{phys}} = 1.225(250) \text{ GeV} \quad (4.11)$$

from method (B) as our main values.

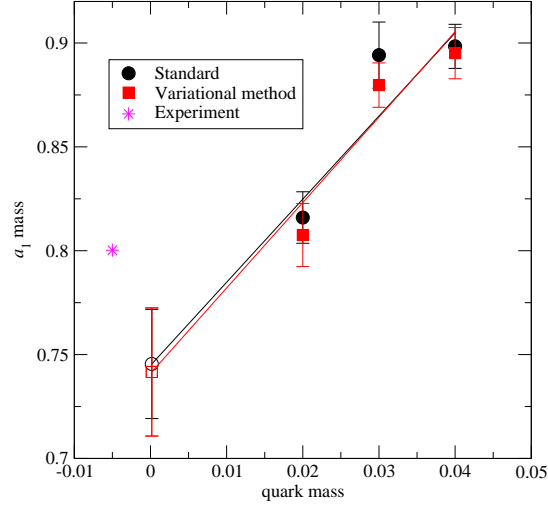


Fig. 18.  $m_{a_1}$  vs  $m_f$ . The asterisk on the left shows the experimental value.<sup>1)</sup>

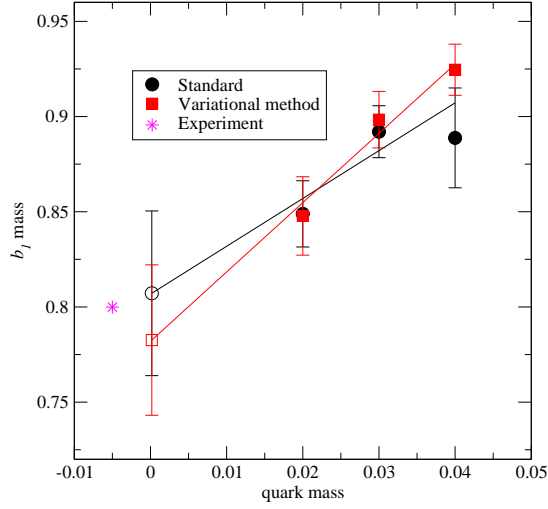


Fig. 19.  $m_{b_1}$  vs  $m_f$ . The asterisk on the left shows the experimental value.<sup>1)</sup>

These numbers may be compared with the experimental results for  $b_1(1235)$ ,  $h_1(1170)$ ,  $a_1(1260)$ , and  $f_1(1285)$ , the first two of which are in good agreement with the numerical results. However further investigations based on realistic settings are clearly needed for more detailed comparisons.

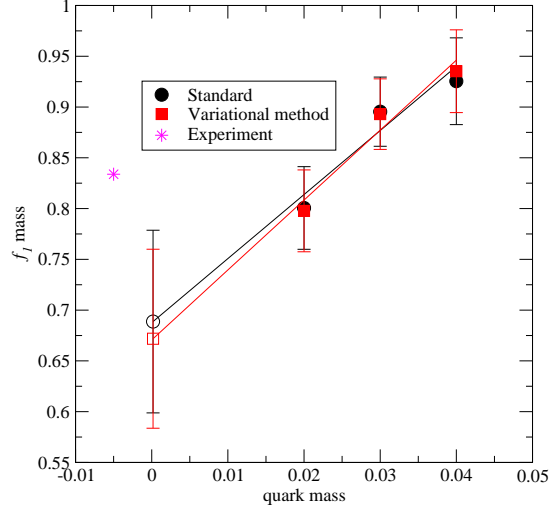


Fig. 20.  $m_{f_1}$  vs  $m_f$ . The asterisk on the left shows the experimental value.<sup>1)</sup>

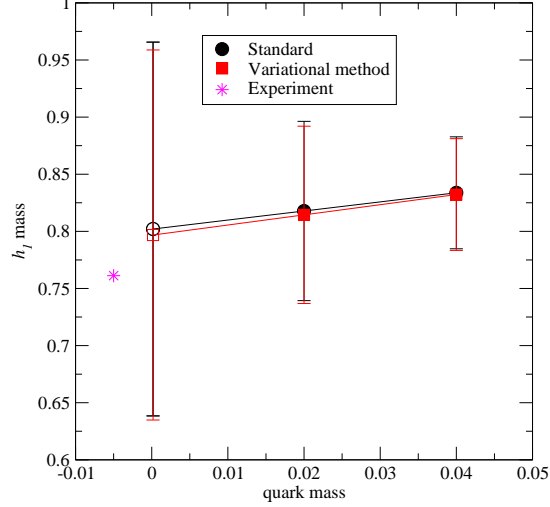


Fig. 21.  $m_{h_1}$  vs  $m_f$ . The asterisk on the left shows the experimental value.<sup>1)</sup>

#### 4.7. Excited meson ( $\pi^*$ , $\rho^*$ ) masses

In this subsection, the second excited states of the pion and  $\rho$  meson are discussed. Using method (B), we extract the eigenvalue for the second excited state,  $\lambda_{O^*}(t)$ ,  $O = \pi, \rho$  eq. (3.52), which is plotted in the right panels of Fig. 22 and 23, respectively. Although we only

Table XVI.  $m_{a_1}$  at the physical quark mass point ( $m_f = m_{u,d}$ ).

$m_{a_1}$	$m_{a_1}^{\text{phys}}$ [MeV]	$m_{a_1} r_0$	method
0.745(26)	1,146(45)	3.19(12)	(A)
0.742(31)	1,140(51)	3.17(14)	(B)

Table XVII.  $m_{b_1}$  at the physical quark mass point ( $m_f = m_{u,d}$ ).

$m_{b_1}$	$m_{b_1}^{\text{phys}}$ [MeV]	$m_{b_1} r_0$	method
0.807(43)	1,241(70)	3.45(19)	(A)
0.783(40)	1,203(64)	3.35(17)	(B)

Table XVIII.  $m_{f_1}$  at the physical quark mass point ( $m_f = m_{u,d}$ ).

$m_{f_1}$	$m_{f_1}^{\text{phys}}$ [MeV]	$m_{f_1} r_0$	method
0.689(90)	1,058(139)	2.95(39)	(A)
0.672(88)	1,033(137)	2.87(38)	(B)

Table XIX.  $m_{h_1}$  at the physical quark mass point ( $m_f = m_{u,d}$ ).

$m_{h_1}$	$m_{h_1}^{\text{phys}}$ [MeV]	$m_{h_1} r_0$	method
0.802(164)	1,233(252)	3.43(70)	(A)
0.797(162)	1,225(250)	3.41(69)	(B)

Table XX.  $m_{\pi^*}$ .

$m_f$	$m_{\pi^*}$	$t_0$	$t_{\min}$	$t_{\max}$	method
0.02	1.215(50)	5	$t_0 + 1$	8	(B)
0.03	1.211(27)	5	$t_0 + 1$	8	(B)
0.04	1.242(26)	5	$t_0 + 1$	8	(B)

use two different operators for each meson, and  $\lambda_{O^*}(t)$  may have a significant contribution from the higher excited state, we fit  $\lambda_{O^*}(t)$  to extract the temporal exponent,  $m_{O^*}$ , or the mass of the excited states using eq. (3.54). The results of the fitting are shown in Tables XX and XXI. We checked that the results for  $t_0 = 5$  and  $t_0 = 6$  are consistent with each other.

We performed linear extrapolation using eq. (3.65) to the physical quark mass point, and found that

$$m_{\pi^*}^{\text{phys}} = 1.791(138) \text{ GeV} , \quad (4.12)$$

$$m_{\rho^*}^{\text{phys}} = 2.028(131) \text{ GeV} \quad (4.13)$$

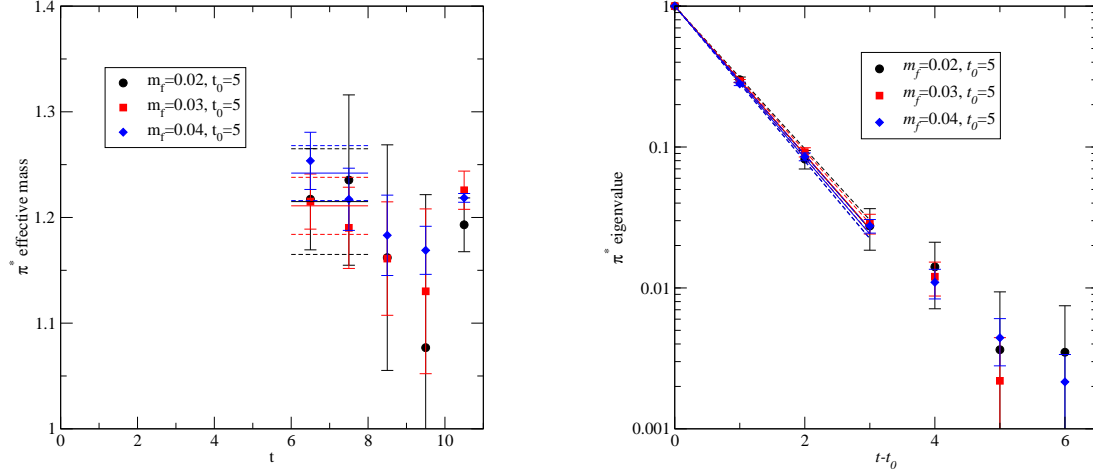


Fig. 22. Effective mass of  $\pi^*$  and eigenvalue as functions of  $t$  and  $t - t_0$ .

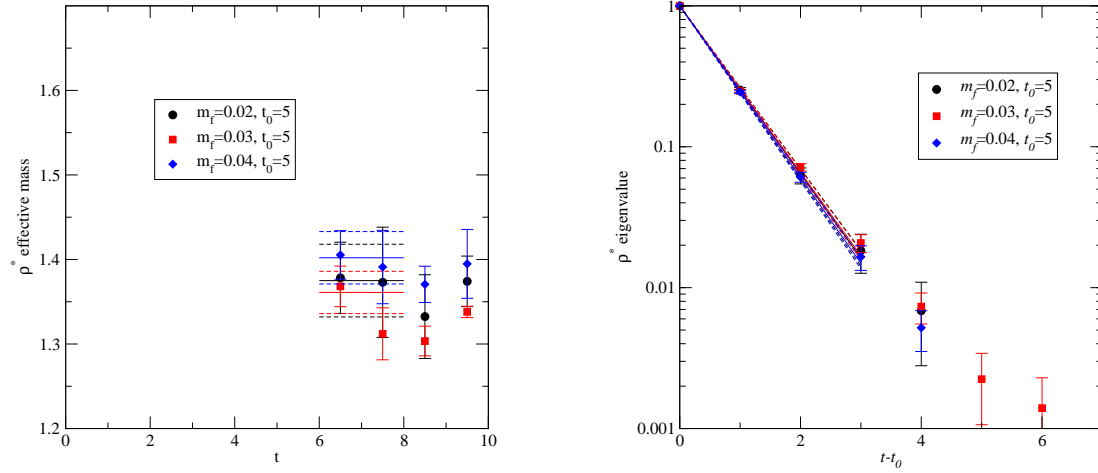


Fig. 23. Effective mass of  $\rho^*$  and eigenvalue as functions of  $t$  and  $t - t_0$ .

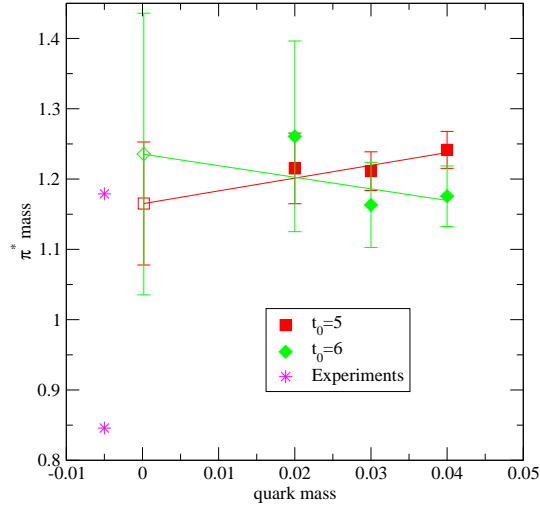
(see Figs. 24 and 25, Table XXII and XXIII). These states may be interpreted as  $\pi(1300)$ , and  $\rho(1450)$  or  $\rho(1700)$ .

#### 4.8. Decay constants

As the last set of numerical results, we present the leptonic decay constant in this subsection. The decay constant of the ground-state pion,  $f_\pi$ , is determined using method (C),

Table XXI.  $m_{\rho^*}$ .

$m_f$	$m_{\rho^*}$	$t_0$	$t_{\min}$	$t_{\max}$	method
0.02	1.375(43)	5	$t_0 + 1$	8	(B)
0.03	1.361(25)	5	$t_0 + 1$	8	(B)
0.04	1.402(31)	5	$t_0 + 1$	8	(B)

Fig. 24.  $m_{\pi^*}$  vs.  $m_f$ . The left most star symbols show the experimental values<sup>1)</sup> in the real world.Table XXII.  $m_{\pi^*}$  at the physical quark mass point ( $m_f = m_{u,d}$ )

$m_{\pi^*}$	$m_{\pi^*}^{\text{phys}}$ [MeV]	$m_{\pi^*} r_0$	method
1.165(88)	1,791(138)	4.98(38)	(B)

Table XXIII.  $m_{\rho^*}$  at the physical quark mass point ( $m_f = m_{u,d}$ )

$m_{\rho^*}$	$m_{\rho^*}^{\text{phys}}$ [MeV]	$m_{\rho^*} r_0$	method
1.319(82)	2,028(131)	5.64(36)	(B)

and fitting the smeared two-point function to formula (3.61). We also fitted the same two-point functions to the double exponential formula (3.63) using the values of  $m_{\pi}$  and  $m_{\pi^*}$  determined from the variational method (method (B)) to investigate the decay constant for the second excited state,  $f_{\pi^*}$ , using method (D).

Table XXIV shows the results for each simulated quark mass. The pion mass and decay

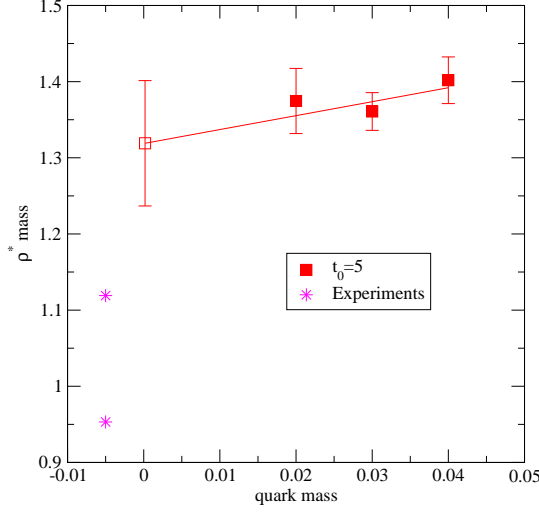


Fig. 25.  $m_{\rho^*}$  vs.  $m_f$  The left most star symbols show the experimental values<sup>1)</sup> in the real world.

Table XXIV.  $f_{\pi}$  and  $f_{\pi^*}$ .

$m_f$	$m_{\pi}$	$f_{\pi}$	$m_{\pi^*}$	$f_{\pi^*}$	$t_{\min}$	$t_{\max}$	method
0.02	0.2936(13)	0.09561(40)	—	—	7	14	(C)
	0.2934(13)(fixed)	0.09540(43)	1.215(50)(fixed)	0.02244(54)	4	14	(D)
	0.2938(18) <sup>a</sup>	0.09494(62) <sup>a</sup>	—	—	9	16	(C)
0.03	0.3598(15)	0.10350(46)	—	—	10	16	(C)
	0.3581(10)(fixed)	0.10370(44)	1.211(27)(fixed)	0.03236(65)	4	16	(D)
	0.3610(18) <sup>a</sup>	0.10253(56) <sup>a</sup>	—	—	9	16	(C)
0.04	0.4098(12)	0.11002(39)	—	—	8	16	(C)
	0.4092(11)(fixed)	0.10964(40)	1.242(26)(fixed)	0.04362(61)	4	16	(D)
	0.4087(16) <sup>a</sup>	0.11059(57) <sup>a</sup>	—	—	9	16	(C)

<sup>(a)</sup> These values are quoted in the previous paper.<sup>25)</sup>

constants are consistent with those reported in the previous paper<sup>25)</sup> within statistical error.

Although the  $\pi^*$  decay constant is poorly numerically determined, an interesting theoretical prediction can be made. AWTI, (3·60), for  $\pi^*$  describes the equation for its decay constant,

$$f_{\pi^*} = \frac{2(m_f + m_{\text{res}})}{m_{\pi^*}^2} \langle 0 | P^a | \pi^* \rangle . \quad (4.14)$$



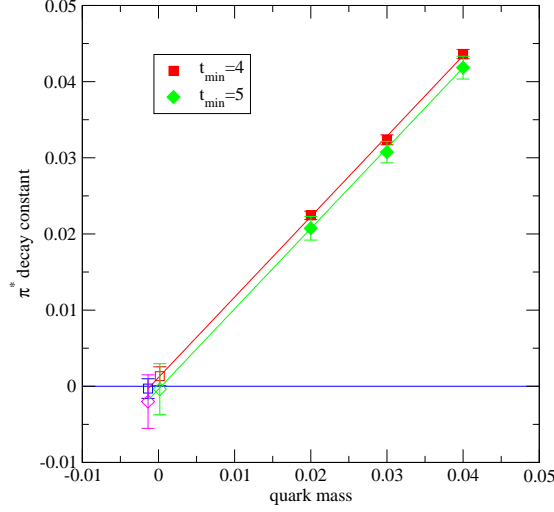


Fig. 26.  $f_{\pi^*}$  vs  $m_f$ .

Table XXV.  $f_{\pi^*}$  at the physical quark mass point ( $m_f = m_{u,d}$ ) and the chiral limit ( $m_f = -m_{\text{res}}$ ).

$m_f$	$f_{\pi^*}$	$f_{\pi^*}^{\text{phys}}$ [MeV]	$f_{\pi^*} r_0$	method
$m_{u,d}$	0.0013(12)	20(19)	0.0057(53)	(D)
$-m_{\text{res}}$	-0.0003(13)	-05(20)	-0.0013(57)	(D)

Table XXVI.  $f_{\rho}/Z_V$ .

$m_f$	$m_{\rho}$	$f_{\rho}/Z_V$	$t_{\text{min}}$	$t_{\text{max}}$	method
0.02	0.5730(96)	0.2011(66)	9	13	(C)
0.03	0.6035(64)	0.2025(50)	10	14	(C)
0.04	0.6448(51)	0.2164(37)	9	14	(C)

If  $m_{\pi^*}$  is not an NG boson, so  $m_{\pi^*}$  remains nonzero, the right-hand side vanishes at the chiral limit, ( $m_f \rightarrow -m_{\text{res}}$ ). This prediction was checked on a lattice QCD using Wilson fermions.<sup>35)</sup> and  $f_{\pi^*}$  was consistent to be zero at the chiral limit.

Figure 26 and Table XXV show the linear extrapolation of  $f_{\pi^*}$ . At the chiral limit, the  $\pi^*$  decay constant is also consistent with the theoretical prediction, *i.e.*,  $f_{\pi^*} \rightarrow 0$ .

Next we discuss the  $\rho$  meson decay constant,  $f_{\rho}$ . The result of the fitting using eq. (3.62) is shown in Table XXVI. The mass of the  $\rho$  extracted by this fitting is consistent with those obtained from methods (A) and (B) within statistical error for all  $m_f$ .

Then the decay constant at the physical quark mass point is obtained as

$$f_\rho^{\text{phys}} = 210(15) \text{ MeV} \quad (4.15)$$

by linear extrapolation (see Table XXVII). The renormalization factor,  $Z_V$ , which converts the lattice operator into the one in the continuum for  $\overline{\text{MS}}$  at  $\mu = 2 \text{ GeV}$  is necessary to obtain a physical value for the decay constants. We use  $Z_A = 0.75734(55)$ , which was determined in the previous paper,<sup>25)</sup> and the relation  $Z_V = Z_A$ , assuming the good chiral symmetry of the current simulation.

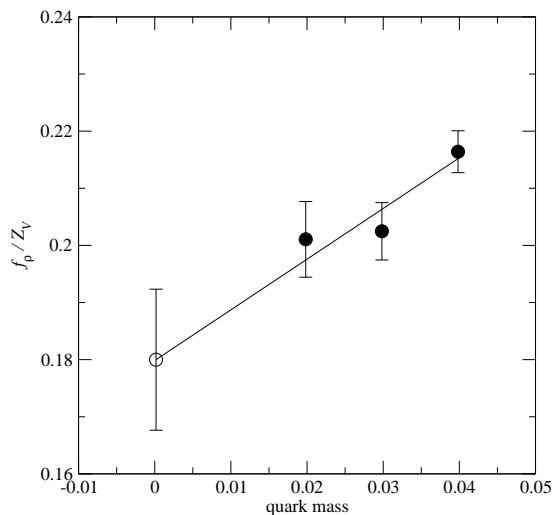


Fig. 27.  $f_\rho/Z_V$  vs  $m_f$ .

Table XXVII.  $f_\rho$  at the physical quark mass point ( $m_f = m_{u,d}$ )

$f_\rho/Z_V$	$f_\rho$	$f_\rho^{\text{phys}}$ [MeV]	$f_\rho r_0$	method
0.1800(123)	0.1363(94)	210(15)	0.0583(41)	(C)

#### 4.9. Systematic uncertainties

So far we have mainly discussed error due to the limited size of the statistical sample. Our numerical results were obtained only at one lattice scale, in one space-time volume, for three quark masses heavier than the physical values, and the strange sea quark was neglected. In this section, various sources of systematic errors are listed and some of their magnitudes are very roughly estimated to compare our results with those of experiments.

- Approximating the continuous space-time by a discrete lattice results in a discretization error. Using DWF, the error starts with  $\mathcal{O}(m_{\text{res}}a) + \mathcal{O}(a^2\Lambda_{\text{QCD}}^2)$ . The value of  $m_{\text{res}}a$  is negligibly small in our simulation compared with the large statistical error involved except in the case of the pion. Our results are closer to their continuum values than those obtained using a Wilson-type fermion on similar lattice scale.

For quenched DWF QCD, the physical values of  $f_\pi$ ,  $f_K$ , and  $f_K/f_\pi$  shift by  $\sim 5\%$ ,  $3\%$ , and  $2\%$ , respectively, when the lattice scale changes from  $a^{-1} = 2 \text{ GeV}$  to continuum limit,<sup>36)</sup> which are equal or less than current statistical error.

- Because of the limited number of quark mass points calculated in our simulation, we restricted ourselves to using the simplest linear chiral extrapolations (3.65) and that obtained from the AWTI (3.64). A more appropriate extrapolation based on a larger number of quark mass points is the chiral fitting formula from the (partially quenched) chiral perturbation theory. While the mass of  $\eta'$ , which is investigated as the main topic in this work, shows little dependence on quark mass, a more precise chiral extrapolation to the physical quark mass point using lighter quark masses is needed to obtain more reliable results.
- Although our assumption, that the ground state is a one-particle state is certainly wrong for some quantum numbers, some of the decay channel in nature are prohibited in simulations using degenerate up and down quarks with heavier mass in a relatively small spatial box  $(2 \text{ fm})^3$  without a strange quark. More sophisticated investigations such as calculating the scattering amplitudes between multiparticles are needed to verify our spectrum results for the decaying meson.
- Without results obtained from a larger volume, it is difficult to estimate the finite-volume effect, although it might be smaller than that for baryons.
- Strange sea quark effect: The number of quark flavors that play dynamical roles in the  $\eta'$  meson may be very important as seen in the WV relation,  $m_{\eta'}^2 \propto N_f$ . By increasing  $N_f$  from 2 to 3 by including strange quark, the WV prediction for  $m_{\eta'}$  becomes  $\sim 20\%$  larger. A strange quark is, however, heavier than up/down quarks, and the mass of  $\eta'$  in the  $N_f = 2 + 1$  QCD is likely to be in between the results of  $N_f = 2$  and 3.
- Topological charge distribution and its effects to  $\eta'$  meson: In our simulation, we deliberately used a special gauge action, DBW2, for good chiral symmetry. However, the autocorrelation time of the topological charge in the simulation becomes longer. The samples taken in our simulation may not be sufficiently long for the reliable estimation of the autocorrelation time for  $Q_{\text{top}}$ . The growth of the binned-jackknife error for  $\langle Q_{\text{top}} \rangle$  with increasing bin size was monitored, and we estimated the autocorrelation time of roughly  $\sim 300$  trajectories for the  $m_f = 0.02$  ensemble and  $\sim$

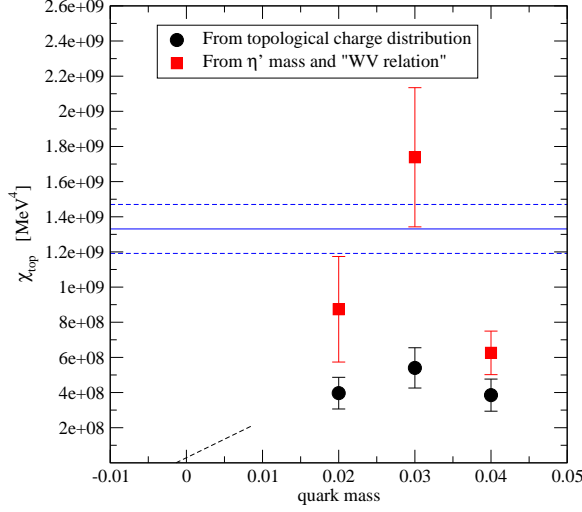


Fig. 28. Circles show the measured  $\chi_{\text{top}}$  as a function of  $m_f^{25),53)}$  while squares show values calculated from  $m_{\eta'}$  and  $m_{\pi}$ , as described in the next section. The horizontal line shows the value obtained from a pure SU(3) YM simulation.<sup>4)</sup> The dotted line shows the prediction from chiral perturbation theory.

200 trajectories for  $m_f = 0.03, 0.04$ . Because of the less frequent tunneling between different topological sectors, the charge distribution sampled in our simulation may be statistically skewed. In fact,  $\langle Q_{\text{top}} \rangle = -0.7(7), 1.4(6)$ , and  $1.8(4)$  for  $m_f = 0.02, 0.03$ , and  $0.04$ , respectively. Note that the central value for  $m_f = 0.04$  is more than four standard deviations away from zero. It is conceivable that this poor sample of the topological sectors causes significant systematic errors in  $\eta'$  spectrum, particularly for the  $m_f = 0.04$  ensemble.

Figure 28 shows the topological susceptibility,  $\chi_{\text{top}}$  in (1.4) as a function of quark mass. The fact that the susceptibility for all three masses is constant within two standard deviations implies that the simulation points are far from the lighter-quark-mass region, where the susceptibility may vanish as a linear function of quark mass. It is also possible the tunneling between different topological sectors does not occur sufficiently frequently, as shown in Figure 29; thus, the estimation for the susceptibility has a larger systematic error.

Of course, more reliable estimation of the magnitude of these systematic errors may be carried out by future simulations on a finer and larger lattice using lighter quark masses with the strange sea quark effect, and with a larger statistical sample size.

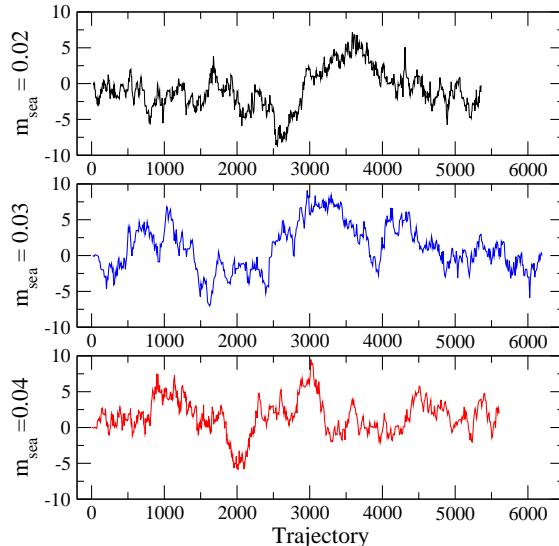


Fig. 29. History of the topological charge in the same simulation as that used for Fig. 28.

## §5. Summary and discussions

We have measured light meson propagators in all channel (flavor nonsinglet/singlet pseudoscalar, vector, scalar, pseudovector, and tensor meson  $\pi$ ,  $\rho$ ,  $a_0$ ,  $a_1$ ,  $b_1$ ;  $\eta'$ ,  $\omega$ ,  $f_0$ ,  $f_1$ ,  $h_1$ ) and estimated the ground state meson masses and some of leptonic decay constants, as well as, the excited state mass, in two flavors of domain wall QCD.

The size of the statistical sample used in the calculation is increased by five to ten times higher than that reported previously.<sup>25)</sup> By applying the gauge-invariant Wuppertal smearing because of quark operators for their better overlap with the ground-state, the statistical error of the pion and  $\rho$  masses is reduced by approximately 50% and the reduction for  $\eta'$  is more than 100%, *i.e.*, we were only able to obtain the nonzero signal by using smeared field. To extract values for the meson mass and decay constant by fitting the propagators, we use two methods, the standard and variational methods. The results of these methods are consistent with each other, which indicates that excited-state contamination of the ground-state is controlled by the smearing.

The systematic uncertainties discussed in the previous section are difficult to estimate; thus, we only quote results with statistical errors. Our results linearly extrapolated to the physical quark mass point are

$$a_{m_\rho}^{-1} = 1.537(26) \text{ GeV} ,$$

$$r_0 = 0.5491(93) \text{ fm}$$

for quantities directly related to the lattice scale,

$$\begin{aligned} f_\rho &= 210(15) \text{ MeV} , \\ f_{\pi^*} &= 20(19) \text{ MeV} \end{aligned}$$

for decay constants, and

$$\begin{aligned} m_{a_0} &= 1.111(81) \text{ GeV} , \\ m_{\eta'} &= 819(127) \text{ MeV} , \\ m_\omega &= 790(194) \text{ MeV} , \\ m_{\pi^*} &= 1.791(138) \text{ GeV} , \\ m_{\rho^*} &= 2.028(131) \text{ GeV} , \\ m_{a_1} &= 1.140(51) \text{ GeV} , \\ m_{b_1} &= 1.203(64) \text{ GeV} , \\ m_{f_1} &= 1.033(137) \text{ GeV} , \\ m_{h_1} &= 1.225(250) \text{ GeV} , \end{aligned}$$

for the mass spectrum. The lattice scale is set from  $m_\rho = 775.49 \text{ MeV}$ .

In Fig. 30, the meson masses obtained in this work are compared with the experimental values.<sup>1)</sup> Horizontal bars show the experimental values and filled circles show the simulation results. The error bars indicate statistical errors only.

The decay constant of the excited pseudoscalar meson turns out to be consistent with zero at the chiral limit as expected:

$$f_{\pi^*} = -05(20) \text{ MeV} . \quad (5.1)$$

The flavor singlet scalar meson,  $f_0$ , was too noisy to obtain its mass in our data.

In this paper we chose the simplest noise method, complex  $\mathbf{Z}_2$ , for evaluating the quark loop amplitudes. More elaborate and/or sophisticated methods<sup>37)–41)</sup> may improve the statistical accuracy of the calculation.

The recalculated pion mass is consistent with the previous result, but the results for  $\rho$  and  $a_0$  meson masses are significantly different. The central value of  $m_\rho$  is 10% larger, *i.e.*,  $a_{m_\rho}^{-1}$  is 10% smaller, and the error bar is reduced by 50% compared with the previous results.<sup>25)</sup> Both the central value and the error bar of  $m_{a_0}$  are 25% smaller than those in previous results.<sup>26)</sup>

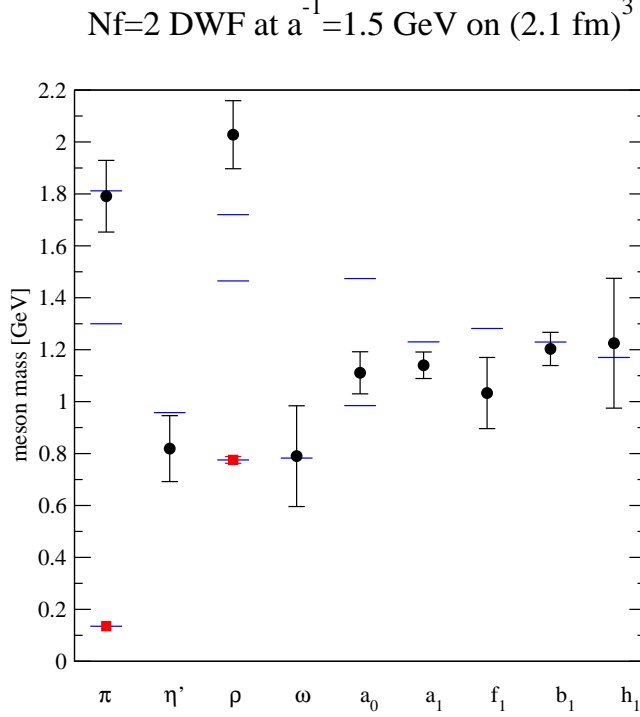


Fig. 30. Comparison of simulation results with experimental values<sup>1)</sup> in the real world. Horizontal bars show the experimental values and filled circles show the simulation results. The error bars indicate statistical errors only. The squares show the quantities used to set the lattice spacing and the physical quark mass point.

We confirm that the flavor singlet pseudoscalar meson,  $\eta'$ , is not an NG boson, and  $m_{\eta'}$  is not likely to be zero at the chiral limit, which is consistent with the standard understanding of the axial anomaly. Assuming the WV relation (1.3) is exact at  $N_c = 3$ , one can calculate the mass gap,  $m_0^2$ , and topological susceptibility,  $\chi_{\text{top}}$ , from our values of  $m_{\eta'}$  and  $m_\pi$ ,

$$\chi_{\text{top}}(\text{WV}) = \frac{f_\pi^2}{2N_f} m_0^2, \quad m_0^2 = m_{\eta'}^2 - m_\pi^2 \quad (5.2)$$

The value of  $\chi_{\text{top}}(\text{WV})$  for  $N_f = 2$  are plotted in Fig. 28 as squares. The horizontal line is  $\chi_{\text{top}}$  obtained from a pure  $SU(3)$  YM simulation.<sup>4)</sup> For  $m_f = 0.02$  and  $0.03$ ,  $\chi_{\text{top}}(\text{WV})$  is consistent with the quenched value, while  $m_f = 0.04$  point  $\chi_{\text{top}}(\text{WV})$  undershoots the line significantly. By linearly extrapolating to the chiral limit, we obtained  $m_0^2 = (808(129) \text{ MeV})^2$  and  $\chi_{\text{top}}(\text{WV}) = (193(15) \text{ MeV})^4$ , which is consistent with the quenched value<sup>4)</sup>  $(191(5) \text{ MeV})^4$ . The agreement, which may imply only small  $1/N_c$  correction, is interesting and deserves further investigation in future.

These results are susceptible to various systematic errors. First, we have only two flavors of dynamical quarks. The omission of the strange quark and antiquark pairs in vacuum,

whose mass is comparable to the dynamical scale of the QCD, may skew our results significantly. The limited number of quark masses, three unitary points, restricted us to examining only the simplest function for the quark mass dependence of the physical results. Thus, the chiral extrapolation has a systematic error due to the omission of curvature resulting from the chiral logarithms and higher order terms although many of our results show little dependence on quark mass. The ensemble was generated only on a  $16^3 \times 32$  lattice with periodic boundary condition in the space directions; thus, all the meson spectrum is affected by the “mirror” images located  $\sim 2$  fm away from the original image in each of the three spatial directions. The effects may be as large as  $\sim 10\%$  for the lightest quark mass points. The lattice discretization error in this study is small,  $\mathcal{O}(m_{\text{res}}a) + \mathcal{O}(a^2\Lambda_{\text{QCD}}^2) \sim \mathcal{O}(1\%)$ . The previous careful studies<sup>25)</sup> on the scaling violation show a  $\sim 5\%$  level shift for  $a \sim 0.1$  fm lattices. The omission of the isospin violation due to the differences in quark mass and electric charge is likely to be negligible compared with other sources of errors, but this issue can also be studied nonperturbatively using lattice.<sup>30)</sup> Despite the significant statistical error and the various remaining systematic uncertainties, this study should serve a benchmark calculation for the statistical features of difficult physical quantities, disconnected diagrams, and computational feasibility tests. The results for the mass of  $\eta'$  were close to the experimental value, indicates that further improvements can be made particularly calculation using an  $N_f = 2 + 1$  DWF ensemble.<sup>33),34)</sup>

## Acknowledgements

We thank RIKEN, Brookhaven National Laboratory, and the U.S. Department of Energy for providing the facilities essential for the completion of this work. We are grateful to members of the RBC collaboration, especially to T. Blum, N. Christ, C. Dawson, R. Mawhinney, K. Orginos, and A. Soni for their various contributions in the early stages of this work and their continuous encouragement. The QCDOC supercomputer at the RIKEN-BNL Research Center (RBRC) was used for the numerical calculations in this work. K.H. thanks RBRC for its hospitality while this work was partly performed. We are grateful to the authors and maintainers of the CPS,<sup>54)</sup> which was used in this work. This work is supported in part by the Grants-in-Aid for Scientific Research from the Ministry of Education, Culture, Sports, Science and Technology (No. 17750050).

## References

- 1) W. M. Yao *et al.* [Particle Data Group], J. Phys. G **33**, 1 (2006).
- 2) E. Witten, Nucl. Phys. B **156**, 269 (1979).



- 3) G. Veneziano, Nucl. Phys. B **159**, 213 (1979).
- 4) L. Del Debbio, L. Giusti and C. Pica, Phys. Rev. Lett. **94**, 032003 (2005) [arXiv:hep-th/0407052].
- 5) S. Itoh, Y. Iwasaki and T. Yoshie, Phys. Rev. D **36**, 527 (1987).
- 6) Y. Kuramashi, M. Fukugita, H. Mino, M. Okawa and A. Ukawa, Phys. Rev. Lett. **72**, 3448 (1994).
- 7) M. Fukugita, Y. Kuramashi, M. Okawa and A. Ukawa, Phys. Rev. D **51**, 3952 (1995).
- 8) V. I. Lesk *et al.* [CP-PACS Collaboration], Phys. Rev. D **67**, 074503 (2003) [arXiv:hep-lat/0211040].
- 9) C. McNeile and C. Michael [UKQCD Collaboration], Phys. Lett. B **491**, 123 (2000) [Erratum-ibid. B **551**, 391 (2003)] [arXiv:hep-lat/0006020].
- 10) C. R. Allton *et al.* [UKQCD Collaboration], Phys. Rev. D **70**, 014501 (2004) [arXiv:hep-lat/0403007].
- 11) T. Struckmann *et al.* [TXL Collaboration], Phys. Rev. D **63**, 074503 (2001) [arXiv:hep-lat/0010005].
- 12) K. Schilling, H. Neff and T. Lippert, Lect. Notes Phys. **663**, 147 (2005) [arXiv:hep-lat/0401005].
- 13) S. Aoki *et al.* [JLQCD Collaborations], PoS **LAT2006**, 204 (2006) [arXiv:hep-lat/0610021].
- 14) L. Venkataraman and G. Kilcup, arXiv:hep-lat/9711006.
- 15) E. B. Gregory, A. C. Irving, C. M. Richards and C. McNeile, PoS **LAT2006**, 176 (2006) [arXiv:hep-lat/0610044].
- 16) S. R. Sharpe, PoS **LAT2006**, 022 (2006) [arXiv:hep-lat/0610094].
- 17) M. Creutz, arXiv:0708.1295 [hep-lat].
- 18) D. B. Kaplan, Phys. Lett. B **288**, 342 (1992) [arXiv:hep-lat/9206013].
- 19) Y. Shamir, Nucl. Phys. B **406**, 90 (1993) [arXiv:hep-lat/9303005].
- 20) V. Furman and Y. Shamir, Nucl. Phys. B **439**, 54 (1995) [arXiv:hep-lat/9405004].
- 21) P. Hernandez, K. Jansen and M. Luscher, Nucl. Phys. B **552** (1999) 363.
- 22) T. Takaishi, Phys. Rev. D **54**, 1050 (1996).
- 23) P. de Forcrand *et al.* [QCD-TARO Collaboration], Nucl. Phys. B **577**, 263 (2000) [arXiv:hep-lat/9911033].
- 24) Y. Aoki *et al.*, Phys. Rev. D **69**, 074504 (2004) [arXiv:hep-lat/0211023].
- 25) Y. Aoki *et al.*, Phys. Rev. D **72**, 114505 (2005) [arXiv:hep-lat/0411006].
- 26) S. Prelovsek, C. Dawson, T. Izubuchi, K. Orginos and A. Soni, Phys. Rev. D **70**, 094503 (2004) [arXiv:hep-lat/0407037].
- 27) S. Gusken, Nucl. Phys. Proc. Suppl. **17**, 361 (1990).

- 28) C. Michael, Nucl. Phys. B **259**, 58 (1985).
- 29) M. Luscher and U. Wolff, Nucl. Phys. B **339**, 222 (1990).
- 30) T. Blum, T. Doi, M. Hayakawa, T. Izubuchi and N. Yamada, arXiv:0708.0484 [hep-lat].
- 31) V. Gadiyak and O. Lottik, Phys. Rev. D **72**, 114504 (2005) [arXiv:hep-lat/0509075].
- 32) C. Dawson, T. Izubuchi, T. Kaneko, S. Sasaki and A. Soni, Phys. Rev. D **74**, 114502 (2006) [arXiv:hep-ph/0607162].
- 33) D. J. Antonio *et al.* [RBC and UKQCD Collaborations], Phys. Rev. D **75**, 114501 (2007) [arXiv:hep-lat/0612005].
- 34) C. Allton *et al.* [RBC and UKQCD Collaborations], Phys. Rev. D **76**, 014504 (2007) [arXiv:hep-lat/0701013].
- 35) C. McNeile and C. Michael [UKQCD Collaboration], Phys. Lett. B **642**, 244 (2006) [arXiv:hep-lat/0607032].
- 36) Y. Aoki *et al.*, Phys. Rev. D **73**, 094507 (2006) [arXiv:hep-lat/0508011].
- 37) J. Foley, K. Jimmy Juge, A. O’Cais, M. Peardon, S. M. Ryan and J. I. Skullerud, Comput. Phys. Commun. **172**, 145 (2005) [arXiv:hep-lat/0505023].
- 38) A. Duncan and E. Eichten, Phys. Rev. D **65**, 114502 (2002) [arXiv:hep-lat/0112028].
- 39) T. A. DeGrand and S. Schaefer, Comput. Phys. Commun. **159**, 185 (2004) [arXiv:hep-lat/0401011].
- 40) C. Michael and J. Peisa [UKQCD Collaboration], Phys. Rev. D **58**, 034506 (1998) [arXiv:hep-lat/9802015].
- 41) S. Collins, G. Bali and A. Schafer, arXiv:0709.3217 [hep-lat].
- 42) C. McNeile and C. Michael [UKQCD Collaboration], Phys. Rev. D **74**, 014508 (2006) [arXiv:hep-lat/0604009].
- 43) K. F. Liu, Prog. Theor. Phys. Suppl. **168**, 160 (2007) [arXiv:0706.1262 [hep-ph]].
- 44) A. Hart, C. McNeile and C. Michael [UKQCD Collaboration], Nucl. Phys. Proc. Suppl. **119**, 266 (2003) [arXiv:hep-lat/0209063].
- 45) T. Burch, C. Gatttringer, L. Y. Glozman, C. Hagen, C. B. Lang and A. Schafer, Phys. Rev. D **73**, 094505 (2006) [arXiv:hep-lat/0601026].
- 46) W. A. Bardeen, A. Duncan, E. Eichten, N. Isgur and H. Thacker, Phys. Rev. D **65**, 014509 (2001) [arXiv:hep-lat/0106008].
- 47) E. B. Gregory, A. C. Irving, C. M. Richards and C. McNeile, arXiv:0709.4224 [hep-lat].
- 48) E. B. Gregory, A. Irving, C. M. Richards, C. McNeile and A. Hart, arXiv:0710.1725 [hep-lat].
- 49) C. Michael and C. Urbach [ETM Collaboration], PoS **LAT2007**, 122 (2007)

- [arXiv:0709.4564 [hep-lat]].
- 50) T. Izubuchi, S. Aoki, K. Hashimoto, Y. Nakamura, T. Sekido and G. Schierholz, PoS **LAT2007**, 106 (2007) [arXiv:0802.1470 [hep-lat]].
- 51) Y. Shamir, Nucl. Phys. B **417**, 167 (1994) [arXiv:hep-lat/9310006].
- 52) T. Blum *et al.*, Phys. Rev. D **66**, 014504 (2002) [arXiv:hep-lat/0102005].
- 53) F. Berruto, T. Blum, K. Orginos and A. Soni, Phys. Rev. D **73**, 054509 (2006) [arXiv:hep-lat/0512004].
- 54) [http://qcdoc.phys.columbia.edu/chulwoo\\_index.html](http://qcdoc.phys.columbia.edu/chulwoo_index.html)